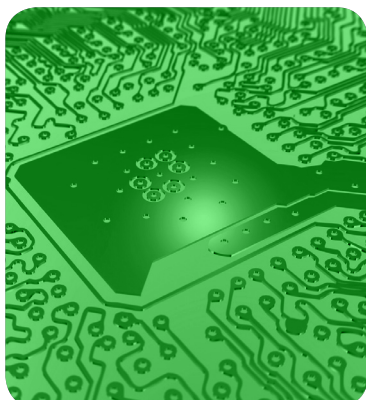


MÁSTERES de la UAM

Facultad de Ciencias
/ 15-16

Química Teórica



**Theoretical study
of NO dissociation
on Ruthenium
surface using
Density Functional
Theory**

Jinggang Lan

Theoretical study of NO dissociation on Ruthenium surface using Density Functional Theory

Jinggang Lan
SUPERVISOR :Dr Yang Wang

Acknowledgements

First of all, I would like to thank Prof. Fernando Martín, Prof. Manuel Alcamí and Dr. Yang Wang for supervising me during these two years of my master.

Part of the work was carried out when I was working with Prof. Coen de Graaf and Prof. Ria Broer in Groningen. I want to acknowledge them and all the group members for their help.

I want to thank Wilson Rodríguez's help from the first day I arrived to the last day in Madrid. He is always very helpful for the problems I have faced.

In addition, I have to thank the Erasmus Mundus Scholarship that enable me to follow the Theoretical Chemistry and Computational Modelling Program in Unversidad Autónoma de Madrid. I want to thank the computing time from Centro de Computación Científica.

Finally, I want to thank my family for always being with me, guiding me, supporting me to realize my dream to be a scientist. I also want to acknowledge all my friends supported me.

1.	INTRODUCTION	6
1.1.	NO on metal surface	6
1.2.	NO over RuO ₂	10
1.3.	Effect of External Electric Field	11
2.	METHODOLOGY	14
2.1.	Introduction of Density functional theory	14
2.1.1.	General Theorems	14
2.1.2.	Local Density Approximation (LDA)	15
2.1.3.	Generalized Gradient Approximation (GGA)	15
2.1.4.	Self Consistent Field (SCF) calculations	15
2.2.	Super-cell model and plane wave basis set.....	16
2.2.1.	Bloch theorem	17
2.2.2.	Plane wave basis set	17
2.2.3.	Pseudo-potential.....	18
2.3.	Stationary Point Optimization.....	20
2.3.1.	Geometry Optimization.....	20
2.3.1.	Transition states search: Nudged Elastic Band (NEB)	20
2.4.	Bader Charge Analysis.....	21
2.5.	Computational details	22
2.6.	Adsorption, activation and dissociative chemisorption energy.....	22
	RESULTS & DISCUSSIONS	24
3.	NO DISSOCIATION ON RU (0001) SURFACE.....	24
3.1.	Ru bulk and surface optimization	24
3.2.	Molecular adsorption of NO.....	26
3.2.1.	Adsorption energies and geometries	26
3.2.1.	Bader Charge Analysis	26
3.3.	Atomic adsorption and diffusion of N and O.....	27
3.3.1.	Atomic adsorption	27
3.3.1.	Atomic species diffusion	28
3.4.	N and O Co-adsorption	29
3.3.1	N-N Co-adsorption.....	30
3.3.2	O-O Co-adsorption	31
3.3.3	N-O Co-adsorption	32
3.5.	NO dissociation	33

3.6.	Implement	34
3.7.	External Electric Field Effect	35
3.7.1.	NO adsorption	35
3.8.2	NO Dissociation	36
4.	STEP EFFECT	38
4.1.	Step model	38
4.2.	Adsorption of Molecular NO	39
4.3.	Atomic Adsorption	40
4.4.	N and O co-adsorption	41
4.5.	NO dissociation on Ru step	41
4.6.	Ru (1019) Terrace effect	43
4.7.	Reconstruction Ru (1019) surface	44
5.	NO DISSOCIATION ON SURFACE (1010)	45
5.1.	Model	45
5.2.	Molecular Adsorption of NO on Ru surface	46
5.3.	NO adsorption transformation	47
5.4.	Atomic adsorption	48
5.5.	Atomic Diffusion	49
5.6.	NO Dissociation	50
6.	THEORETICAL STUDY OF CUBANE-TYPE [Ni ₄ Cl ₈] COMPLEXES' MAGNETIC PROPERTIES	54
6.1.	Research Motivation	54
6.2.	Theoretical background	54
6.2.1.	Heisenberg Hamiltonian	54
6.2.2.	Electronic configurations	55
6.2.3.	Ni ₂ Zn ₂ and NiZn ₃ model	56
6.3.	Molecular Results	57
6.3.1.	Ni _μ ₃ – ClClHL · S _x (x = 0, 4) Result	57
6.3.2	Ni _μ ₃ – ClClHL · S _x (x = 1, 2, 3) Result	58
6.4.	Ni _μ ₃ – ClClHL · S _x (x = 1, 2, 3) adsorption on Au (111) surface	61
6.4.1.	Au bulk and surface optimization	61

6.4.2. Ligand adsorption	61
6.4.3. Niμ3 – ClClHL · Sx (x = 1, 2, 3) adsorption	62
6.5. Conclusion	63
CONCLUSIONS	64
REFERENCE:	66

1. Introduction

Environmental issues come to our eyesight again since the 2015 United Nations Climate Change Conference, reaching a global agreement on the reduction of climate change, the text of which represented a consensus of the representatives of the 196 parties attending it[1]. In this conference, the expected key result was an agreement to set a goal of limiting global warming to less than 2 degrees (°C) compared to pre-industrial levels.

Meanwhile, the unbelievable shocking news was disclosed that the Volkswagen and other vehicles companies admitted to install a hidden software which is specialized to reduce the exhausted emission from the tailpipe when examining the US clean air act standards. The allegations cover approximately 482,000 vehicles sold in the United States over the past seven years [2]. However, Volkswagen, as a European car company, is hard to convince the public that they have completely obeyed clean air standards in Europe. It is also astonishing that such a successful company with good reputation gambled risk on that.

Why? Simple answer: Everything is worth its own price. To lower the price of the catalyst cost, one way is to improve its efficiency, meanwhile another way is to find cheap catalyst to replace noble metal catalyst. NO_x are the primary pollutants of the atmosphere, responsible for environmental problems like fine particles, photochemical smog, acid rain, tropospheric ozone, ozone layer depletion, eutrophication and even global warming. The catalytic abatement of NO_x is one of the major challenges in environmental catalysis [3].

Under current situation, it is urgent to discover a more efficient way to remove nitrogen oxides(NO_x) produced from vehicles which is responsible for various environmental problems. To find a brand new catalyst, it is important to understand the detailed mechanisms of NO_x catalytic dissociation, covering the following issues: 1. catalyst surface relaxation and its electronic structure; 2. NO_x favorable adsorption sites; 3. dissociation barriers and reaction pathways; 4. activation energy and reaction rate of NO_x; 5. effect of coverage; 6. effect of surface steps, doping and defects; 7. effect of temperature and external electric field.

1.1. NO on metal surface

Steps are generally found to possess better reaction activity than terraces [2,4,6,7].

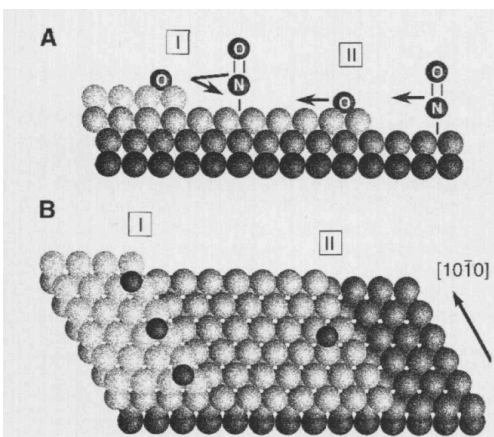


Fig 1.1 Schematic dissociation of NO_x on Ru steps

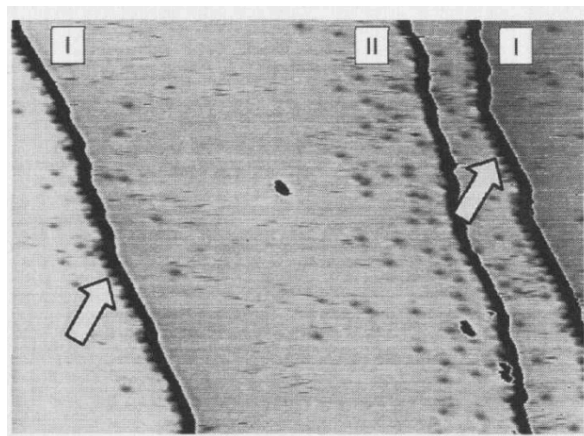


Fig 1.2 STM image of Ru step surfaces[7]

A clean Ru (0001) surface in ultrahigh-vacuum condition was used to dissociate NO molecule around 300K condition. Using scanning tunneling microscope (STM), the NO molecule prefers to dissociate at steps on a Ru (0001) surface as shown in Fig 1.1 & 1.2[7]. The low-coordinated, top Ru metal atoms of atomic steps were identified as the active sites for the NO dissociation.

B.Hammer investigated NO bond activation at a corrugated Ru (0001) surface using PBE, PW91 and RPBE functionals based on Density functional theory (DFT) [3,4]. Monatomic steps in the Ru surface are found to offer completely new reaction pathways with highly reduced energy barriers compared to reactions at a flat surface.

For the flat Ru (0001) surface, slabs of five Ru atomic layers are repeated periodically in a c(4x4) super cell geometry. Hammer's result showed that hcp site in the flat Ru (0001) surface is the most favorable position for NO molecule adsorption ($E_{ad} = -2.64$ eV). Followed by fcc site (-2.40 eV), bridge site (-2.32 eV) and the least top site (-2.06 eV), respectively. Atomic single atom adsorption energy regarding to N and O atoms (with respect to $\frac{1}{2}N_2(g)$ and $\frac{1}{2}O_2(g)$) were also calculated and suggested that hcp site are both most favorable site for N atom (-0.45 eV) and O atom (-2.16 eV). The diffusion of the N and O atom possesses insignificant barriers from fcc site to hcp site which are around 0.3 eV in both cases, while the backward process (hcp to fcc) is not as easy as forward for which energy barriers are 0.79 eV for N atom and 0.5 eV for O atom.

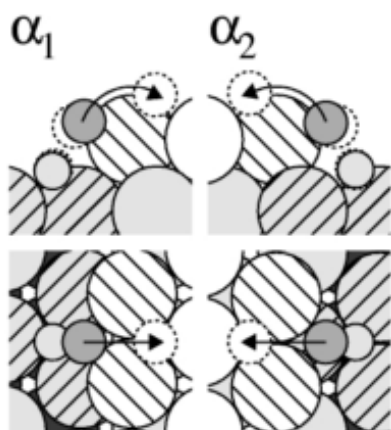


Fig 1.3 Dissociation process at step edges [2], dark one is O atom, light one is N atom

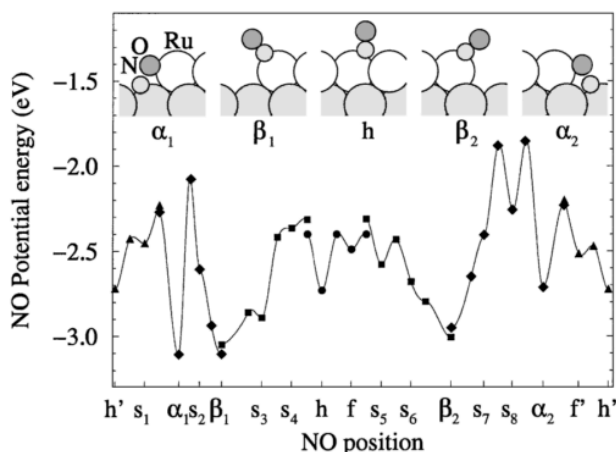


Fig 1.4 Potential energy variation of NO on different positions [2]

The dissociation of NO on a flat surface is hindered by a barrier of 1.28eV. On a corrugated surface, however, the dissociation at the step edges is hindered only by barriers as low as 0.15 eV and 0.17 eV (α_1 and α_2) (Fig. 1.3). The reduction of the energy barrier for NO dissociation at the step edges is so large that rather the diffusion of NO to the step edge than the dissociation of NO becomes a rate limiting step. The diffusion energy barriers for NO moving from the flat Ru (0001) (sites h or h0) to the step edges (sites a or b) are about 0.5 eV (Fig. 1.4) indicating, however, that diffusion to the step edges is still facile compared to dissociation at the flat Ru(0001)

Since the N_2 activation on Ru (0001) forming atomic N atoms is the backward reaction of the N_2 recombination which is the last stage for the NO reduction over Ru (0001) surface. Thus, it is also necessary for us to understand how N_2 molecule activate on Ru (0001) surface. Also, the O_2 dissociation on metal surface could help us learn more about NO dissociation.

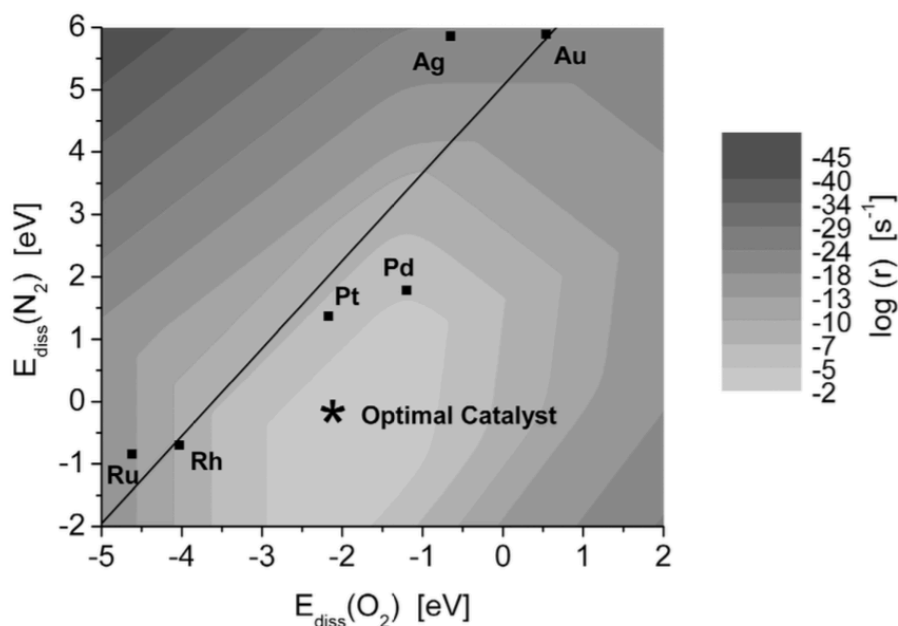


Fig 1.5 Theoretically predicted decomposition rate as a function of the dissociative chemisorption energies of N_2 and O_2 . [8]

The full potential energy diagram for the direct NO decomposition reaction over stepped transition-metal surface was investigated combining an adsorption energies database known as Bronsted-evans-Polanyi (BEP) relations for the activation barriers of diatomic molecule over metal surface. Everything is two-sided, the high reacting activity over steps brings both advantages and problems. To discover optimal catalyst is to balance the advantages and its problems, and find the most optimized catalyst in specific situation.

J.K Norskov [8] concluded that, concerning the direct decomposition of NO on transition metals, Au and Ag possess no significant reactivity for NO dissociation, while Rh and Ru will be poisoned by strongly binding O atoms (especially on the most active step sites). Pd and Pt seem to be the best option in the pure metal surfaces, but cannot be useful in real world like lean-burn conditions.

J.K Noskov also studied the role of steps in N_2 activation on Ru (0001) surface [6]. The adsorption experiments and DFT results showed that N_2 dissociation on the Ru (0001) surface is totally dominated by steps. The origin of the lower barrier of the N_2 dissociation comes from the combination of electronic and geometrical effects. That indicates when the atomic N atoms is going to form molecule N_2 , it might not tend to form around steps but flat area instead.

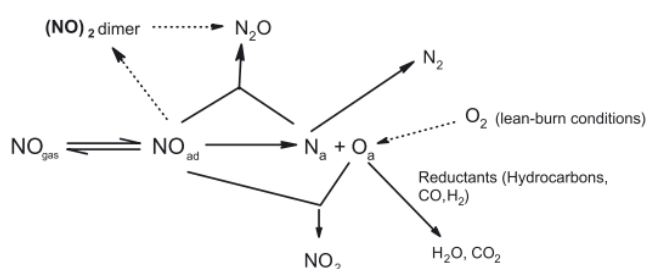


Figure 1.6 General mechanism of NO reduction on transition metal surfaces. [12]

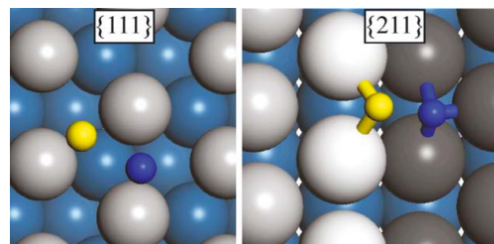


Figure 1.7 TS structures of NO dissociation on the close-packed {1 1 1} surface and the stepped {2 1 1} surface. [12]

P. Hu reviewed the accumulated theoretical results on NO reduction over metal surfaces [10]. There are two types of NO removal that are important. The first one is under a reductive environment, the NO reduction with CO, H₂ or NH₃, which can be efficiently done by traditional three-way catalysts. While the other type is under lean-burn conditions (O₂-rich conditions). The mechanism of NO reduction on transition metals is expected to follow the scheme shown in Figure 1.7, while the mechanism on noble metal based catalysts is less certain since NO dissociation is believed to be unlikely on noble metals [12].

NO dissociation is highly structure sensitive. The comparison between flat surface and step surfaces can be achieved by comparing the TS of NO dissociation on these two surface, as shown in Figure.1.7. In the transition state on the flat surface, three (or four) metal atoms are involved in the N-O dissociation process, while five atoms are involved in the TS on the step surface.

Table 1.1 Calculated Adsorption Energy (E_{ad})^a of NO, N, and O on the Most Stable Sites, and the Barriers (E_a) for the Elementary Reactions on Ir and Pt [12]

		Ir{211}	Ir{111}	Pt{211}	Pt{111}
E_{ad}	NO	3.14	2.10	2.44	2.05
	N	5.51	5.16	4.50	4.45
	O	5.39	4.73	4.31	4.00
E_a	NO→N+O	1.19	1.46	1.70	2.60
	N+N→N ₂	1.81	2.60	1.07	2.72
	NO+N→N ₂ O	2.31	1.33	1.66	1.78
	NO+O→NO ₂	2.56	1.46	1.95	1.52

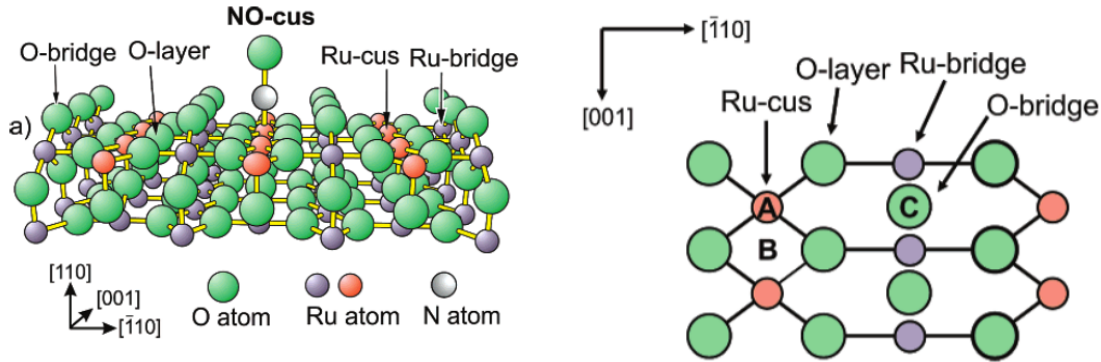
^a The units are eV

David A.King etc. have systematically studied the NO reduction process on Ir and Pt metals. Both flat (111) and the stepped (211) surface of the two metals have been studied for the NO dissociation, N₂ formation, N₂O formation and NO₂ formation. The most stable transition state (TS) for the reaction and its energy barrier is listed in Table 1.1. The results show that NO dissociation prefers to take place on the step rather than on the flat surface for both metal. And the stepped-Ir surface is found to possess high reactivity for NO reduction.

1.2. NO over RuO₂

T.S. Rahman [15,16] reported results of DFT calculation of the interaction of NO with RuO₂ (110) surface that provided further understanding of the experimental observation. The adsorption configurations and their corresponding adsorption energy are given in Table 1.2.

Table 1.2. Calculated Adsorption energy of NO on different site on RuO₂



Adsorption structure side view

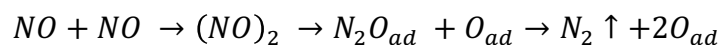
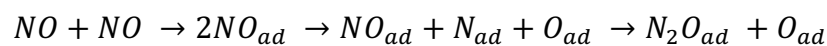
Adsorption structure top view

Adsorption site	Coverage	Adsorption energy	
		Without zero-point energy	With zero-point energy
A: on top of Ru-cus	1 ML	1.61 eV	1.49 eV
	0.5 ML	1.72 eV	1.60 eV
B: bridge site	1 ML	0.47 eV	0.38 eV
C: on-top of O-bridge	1 ML	0.82 eV	0.74 eV
	2 ML	0.74 eV	0.66 eV

Experimentally, no evidence shows that NO can be oxidized to NO₂ over RuO₂ (110) surface, while CO is oxidized to CO₂ on RuO₂ (110) surface even at room temperature [15,16]. DFT results showed that the origin of the fact that NO cannot be oxidized to NO₂ on RuO₂ (110) surface comes from the high desorption energy of NO₂ and very low energy barrier of 0.37 eV for NO₂ to dissociate to NO and O backward, while for the energy barrier of NO + O = NO₂ is 1.22 eV.

As for NO direct dissociation, they found a transition state with energy barrier of 3.22 eV to dissociate NO molecule into N and O atoms, while only 1.72 eV for NO molecule to desorb, that confirm that NO dissociation is not on RuO (110) surface.

In the experiments of Wang [17], at higher exposure, they detected a small amount of N₂O formed, and they proposed the following mechanism:



The energy profile for these reactions are shown in Figure 1.8 below.

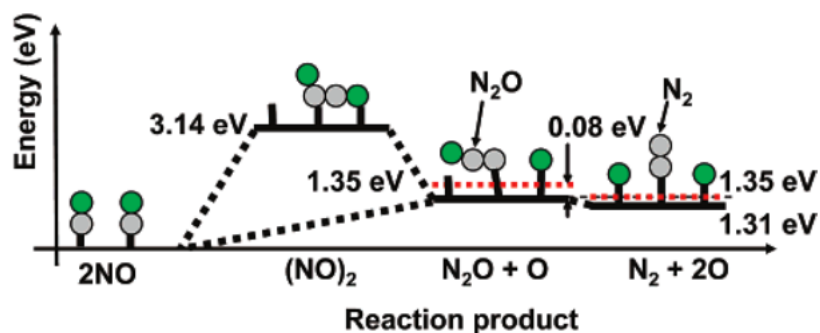


Figure 1.8 Schematic model of the intermediate products and the total energy change for N₂O formation. Desorption level is marked as a dotted line.

According to the DFT calculation results [13], the NO barely dissociate over RuO₂ surface, which doesn't support the first mechanism proposed. Their calculated energy profile for the second reaction mechanism may explain the N₂O production on the surface.

More DFT calculation concerning adsorption and reactions of NO_x on RuO₂(110)[14] showed similar results to previous studies. In addition, they suggested that adsorbed NO (nitrosyl) and to a lesser extent NO₃ (nitrate) dominate the surface phase diagram.

2. Methodology

2.1. Introduction of Density functional theory

2.1.1. General Theorems

In 1960s, Hohenberg, Kohn [29] and Sham proposed Density Functional Theory (DFT), based on the idea that a total energy of the system could be described as a functional of electron density $\rho(\mathbf{r})$. The origin of DFT was attributed by Thomas and Fermi's work in 1927, which assume that the energy of whole system could be written as a functional of electron density, but without exchange energy term. DFT provides the theoretical foundation for converting multi-electron system problem into single-electron equation. That is a powerful tool to calculate electronic structure and total energy of molecule and solid state matter.

DFT is nowadays widely used in many different research areas, including computational chemistry, catalysis, materials, physics. The Hohenberg-Kohn theorems can be summarized as:

- i) The full many-particle ground state system can be described as a unique functional of electron density.
- ii) The total energy of the system has a minimum value which is the correct ground-state energy associated with the electron density.

From the electron density, $\rho(\vec{r})$, all other properties of the system are determined and the total energy E is calculated using

$$E[\rho(\vec{r})] = T_{KS}[\rho(\vec{r})] + \frac{1}{2} \int \int \frac{\rho(\vec{r})\rho(\vec{r}')}{|\mathbf{r}-\mathbf{r}'|} d\mathbf{r}d\mathbf{r}' + \int v_{nuci}(\mathbf{r})\rho(\vec{r})d\mathbf{r} + E_{XC}[\rho(\vec{r})] \quad (2.1.1)$$

where the first term $T_{KS}[\rho(\vec{r})]$ is the kinetic energy of fictitious, non-interacting electrons and is obtained from the single-electron Kohn-Sham equations

$$\left(\frac{-\hbar^2}{2m}\nabla + v_{eff}\right)\psi_i = \varepsilon_i\psi_i \quad (2.1.2)$$

where v_{eff} is the effective field defined by the nuclei and the current electron density. The second and the third term describe electrostatic electron-electron interaction and electron-nuclei interactions, respectively. The last term, E_{XC} , in the total energy equation depends on the unknown exchange-correlation functional.

The fundamental philosophy of Density Functional Theory is to use particle density functional to describe atoms, molecules and solid state matter ground state physical properties.

2.1.2. Local Density Approximation (LDA)

The simplest approximation proposed by Kohn and Sham [30] is the Local Density Approximation. Based on homogenous electron gas theory, the LDA add exchange energy term for the electron density where $E_{XC}[\rho(\vec{r})]$ can be expressed as

$$E_{XC}^{LDA}[\rho(\vec{r})] = \int dr \epsilon_{XC}[\rho(\vec{r})] \rho(\vec{r}) \quad (2.1.3)$$

where $E_{XC}[\rho(\vec{r})]$ is the homogenous electron gas exchange correlation energy. This approximation is strictly tenable when the electron is equally distributed. The LDA works remarkably well for bulk materials where the electron density varies not significantly, but has insufficient accuracy for most application in chemistry, including atoms, molecules, clusters and surfaces.

2.1.3. Generalized Gradient Approximation (GGA)

An extension to the LDA is the generalized gradient approximation (GGA) [31,32], which depends not only on the local density but on the density gradient.

$$E_{XC}^{GGA}[\rho(\vec{r})] = \int dr \epsilon_{XC}[\rho(\vec{r})] \rho(\vec{r}) F_{XC}[\rho(\vec{r}), \nabla \rho(\vec{r})] \quad (2.1.4)$$

Where F_{XC} is enhancement factor. Since the gradient correction can be expressed a GGA functional in various ways, different GGA functionals regarding different properties interest exist. The most popular functionals are the Perdew-Wang 91 (PW91) and the Perdew-Burke-Ernzerhof (PBE) functional.

Compared to LDA calculation results, GGA (1) can describe atoms, molecules, cluster and surface better for their ground state properties; (2) has better accuracy for 3d transition metal than LDA description; (3) gives more reasonable result for 3d transition metal magnetic properties.

2.1.4. Self Consistent Field (SCF) calculations

In many-electron system, for a given initial guess of electron density $\rho(\vec{r})$, the energy of each terms in Eq. (2.1.1) can be obtained, as well as v_{eff} . Using calculated v_{eff} to solve the K-S equation, each term in the total energy and its corresponding wave function can be calculated, and give out a new electron density $\rho(\vec{r})$. If the new electron density is different from the previous electron density, repeat the process until the electron density is converged to a given criteria, as shown in the Figure 2.1.

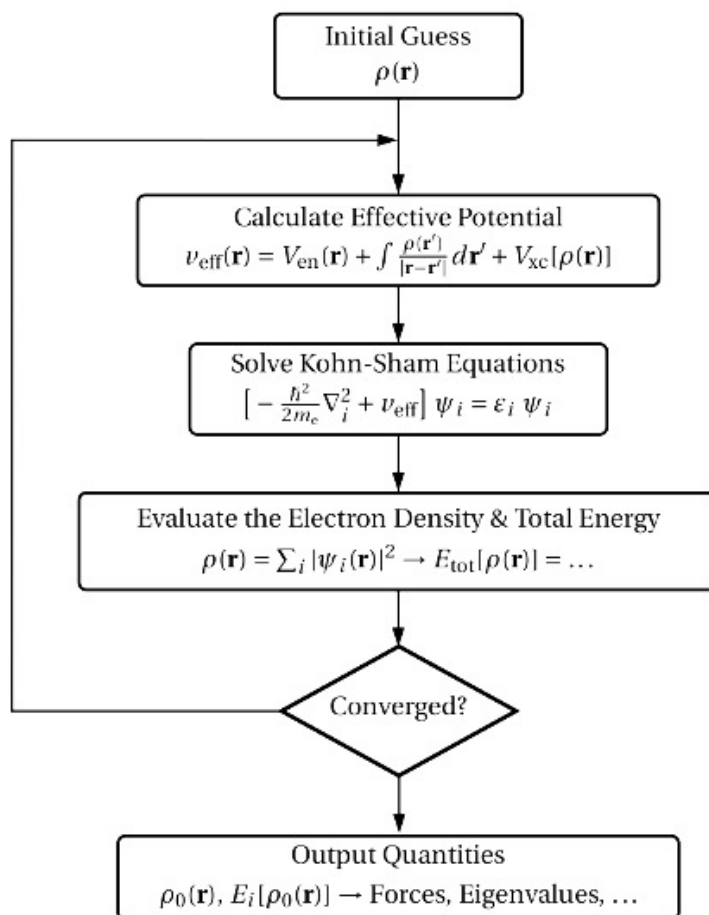


Figure 2.1: A flow chart of the iteration scheme.

At first, an initial guess for the electron density is assumed, which is required for the calculation of v_{eff} , the diagonalization of the Kohn-Sham equations, and the subsequent evaluation of $\rho(\vec{r})$ along with E_{tot} . As long as the convergence criterion is not fulfilled, the numerical procedure is continued with the last $\rho(\vec{r})$ instead of the initial guess. When the criterion is satisfied, various output quantities are computed.

2.2. Super-cell model and plane wave basis set

In realistic system, there are more than 10^{20} atoms in cubic millimeter, which is unaffordable to treat by current numerical method. At this scale, the systems are periodic.

To build the model for the surface, there are two methods: cluster model and super-cell model. Both methods are widely used to study surface science and molecule adsorption.

Cluster model method assume that the bond between the adsorbates and surface is localized. However, the electron configuration for the surface could be highly delocalized, and results show that the size of the cluster has a significant influence on reaction activity. Thus, how to select a proper cluster model should be careful.

Compared to the cluster model, the super-cell model is conceptually easier, as the surface is modelled using a unit cell periodically repeated in all three dimensions.

2.2.1. Bloch theorem

For a three-dimensional periodic system, the potential energy is a function of lattice periodicity. Bloch theorem suggests that electron wave-function is a harmonic plane wave conducted in accordance with the lattice periodicity, where

$$\psi_i(\vec{r}) = f_i(\vec{r})e^{ik\vec{r}} \quad (2.2.1)$$

the harmonic term of wave-function can be expressed as discrete plane wave in reciprocal space

$$f_i(\vec{r}) = \sum_{\mathbf{g}} c_{i,\mathbf{g}} e^{i\mathbf{g}\vec{r}} \quad (2.2.2)$$

Thus, the three-dimensional electron wave function can be expressed as plane wave using,

$$\psi_i(\vec{r}) = \sum_{\mathbf{g}} c_{i,\mathbf{g}} e^{i(\mathbf{g}+\mathbf{k})\vec{r}} \quad (2.2.3)$$

For a three-dimensional periodic system, the first Brillouin zone is a restricted set of k-vectors with the property that no two of them are equivalent, yet every possible k is equivalent to one (and only one) vector in the first Brillouin zone. Thus, if we restrict k to the first Brillouin zone, then every Bloch state has a unique k. Therefore, the first Brillouin zone is often used to depict all the Bloch states without redundancy.

2.2.2. Plane wave basis set

A periodic system is assumed to be placed in a unit cell defined by the unit vectors $\vec{a}_1, \vec{a}_2, \vec{a}_3$. The volume of the unit cell is $\Omega = [\vec{a}_1, \vec{a}_2, \vec{a}_3] = \vec{a}_1 \cdot (\vec{a}_2 \times \vec{a}_3)$

It is easy to show from the periodicity constraint that the wave-vectors can be defined in terms of the following reciprocal lattice vectors.

$$\vec{b}_1 = 2\pi \frac{\vec{a}_2 \times \vec{a}_3}{\Omega} \quad (2.2.4)$$

$$\vec{b}_2 = 2\pi \frac{\vec{a}_3 \times \vec{a}_1}{\Omega} \quad (2.2.5)$$

$$\vec{b}_3 = 2\pi \frac{\vec{a}_1 \times \vec{a}_2}{\Omega} \quad (2.2.6)$$

wave-vectors that satisfy the periodicity of the lattice

$$\vec{G}_{i_1 i_2 i_3} = \left(i_1 - \frac{N_1}{2}\right) \vec{b}_1 + \left(i_2 - \frac{N_2}{2}\right) \vec{b}_2 + \left(i_3 - \frac{N_3}{2}\right) \vec{b}_3 \quad (2.2.7)$$

The exact form of the plane-wave expansion used in plane wave code is

$$u_n(\vec{r}) = \frac{1}{\sqrt{\Omega}} \sum_{i_1=1}^{N_1} \sum_{i_2=1}^{N_2} \sum_{i_3=1}^{N_3} \tilde{u}_n(\vec{G}_{i_1 i_2 i_3}) e^{i\vec{G}_{i_1 i_2 i_3} \vec{r}} \quad (2.2.8)$$

The upper-limits of the summation N_1, N_2, N_3 control the spacing of the real-space grid

$$\vec{r}_{i_1 i_2 i_3} = \left(\frac{i_1}{N_1} - \frac{1}{2}\right) \vec{a}_1 + \left(\frac{i_2}{N_2} - \frac{1}{2}\right) \vec{a}_2 + \left(\frac{i_3}{N_3} - \frac{1}{2}\right) \vec{a}_3 \quad (2.2.9)$$

There is a further truncation of plane wave expansion in plane-wave calculations. Namely, only the reciprocal lattice vectors whose kinetic energy lower than a predefined maximum cutoff energy,

$$\frac{1}{2} |\vec{G}|^2 < E_{cut}(\text{wavefunction cutoff energy}) \quad (2.2.10)$$

are kept in the expansion, while the rest of the coefficients are set to zero.

Since the density is the square of the wave-functions, it can vary twice as rapidly. Hence for translational symmetry to be formally maintained the density, which is also expanded using plane-waves

$$\rho(\vec{r}) = \sum_n u_n^*(\vec{r}) u_n(\vec{r}) = \sum_{\vec{G}} \rho(\vec{G}) e^{i\vec{G}\cdot\vec{r}} \quad (2.2.11)$$

Should contain 4 times more plane-waves than the corresponding wave-function expansion

$$\frac{1}{2} |\vec{G}|^2 < 4E_{cut}(\text{Density cutoff energy}) \quad (2.2.12)$$

In solid-state systems, the plane-wave expansion given by

$$u_n(\vec{r}) = \frac{1}{\sqrt{\Omega}} \sum_{\vec{G}} \widetilde{u}_n(\vec{G}) e^{i\vec{G}\cdot\vec{r}} \quad (2.2.13)$$

is not complete. Based on the fact that the translation operators $T(\mathbf{R})$ are compatible with the Hamiltonian of the system. $[T(\mathbf{R}), H] = 0$, and that not all eigenkets of $T(\mathbf{R})$ can be expanded strictly in terms of the set of eigenkets $|u_n\rangle$. The wave-function expansion can be generalized based on Bloch's Theorem

$$|\vec{k}, n\rangle = |\vec{k}\rangle |u_n\rangle \text{ or } \Psi_{\vec{k},n}(\vec{r}) = e^{i\vec{k}\cdot\vec{r}} u_n(\vec{r}) \quad (2.2.14)$$

Where \mathbf{k} are all the allowed wave-vectors in the primitive cell of the reciprocal lattice.

2.2.3. Pseudo-potential

The pseudopotential method [33,34,35] is based on two observations, the core orbitals and valence orbitals. In pseudopotential approximation the original atoms that constitute a given chemical system are modified by removing core energy levels and enforcing the Pauli exclusion principle via repulsive pseudopotential. This removes the wiggles from the atomic valence orbitals and allows efficient application of plane wave basis set expansion.

For a given multi-atoms solid system, based on different properties of wave-functions, the space coordinates can be divided into two part:

- 1 Core states, that its wave-function has little or ignorable interaction with neighboring atoms' wave-function
- 2 Valence electrons, that their wave-functions can overlap and interact with each other.

Use $|\psi_c\rangle$ and $|\psi_v\rangle$ to express the precise Wave-function of core state and valence electron, their eigenvalue are ε_c and ε_v , respectively.

$$H|\psi_c\rangle = \varepsilon_c |\psi_c\rangle \quad (2.2.15)$$

$$H|\psi_v\rangle = \varepsilon_v |\psi_v\rangle \quad (2.2.16)$$

Then

$$|\psi_v\rangle \geq |\psi_v^{PS}\rangle + \sum_c \beta_c |\psi_c\rangle \quad (2.2.17)$$

Where

$$\beta_c = -\langle \psi_c | \psi_v^{PS} \rangle \quad (2.2.18)$$

Substituting this expression in the Schrodinger equation gives

$$H|\psi_v^{PS}\rangle + \sum_c (\varepsilon_v - \varepsilon_c) |\psi_c\rangle \langle \psi_c | \psi_v^{PS} \rangle = \varepsilon_v |\psi_v^{PS}\rangle \quad (2.2.19)$$

so that the smooth pseudo-state obeys a Schrodinger equation with an extra energy-dependent non-local potential

$$(T + U)|\psi_v^{PS}\rangle = \varepsilon_v |\psi_v^{PS}\rangle \quad (2.2.20)$$

Thus,

$$U = V + \sum_c (\varepsilon_v - \varepsilon_c) |\psi_c\rangle \langle \psi_c | \quad (2.2.21)$$

The potential U, whose effect is localized in the core, is so-called pseudo-potential, which gives the wave-function of electron motion under this potential.

The Figure 2.2 gives the Schematic diagram of the relationship between all-electron and pseudo-potentials and wave-functions. From the diagram, when $r > r_c$, the wave-function of the all-electron and pseudo-potential are almost identical; when $r < r_c$, the wave-function of the pseudo-potential change slowly.

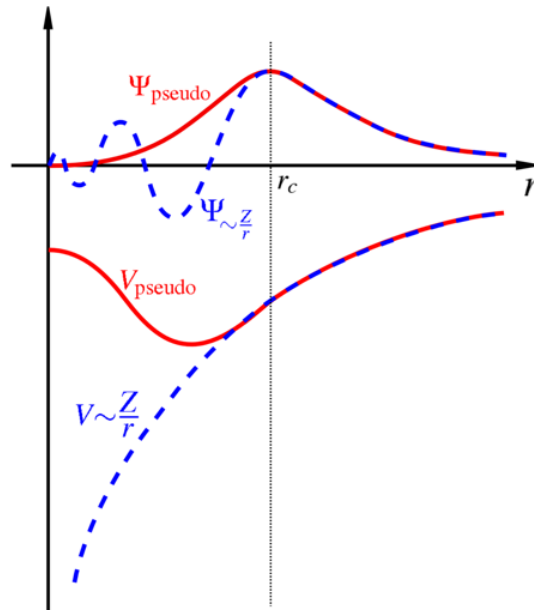


Figure 2.2. Comparison of a wavefunction in the Coulomb potential of the nucleus (blue) to the one in the pseudopotential (red). The real and the pseudo wavefunction and potentials match above a certain cutoff radius r_c .

2.3. Stationary Point Optimization

2.3.1. Geometry Optimization

To make sure that the energy minimum we search in the potential energy surface is the global minimum but not local minimum, the powerful searching algorithm to calculate the atoms movement to the most stable position is needed. The most widely used method are steepest descent, conjugate gradient method (CG), quasi-newton method etc [36,37]. The Figure give the pathway for different algorithms for the optimization method.

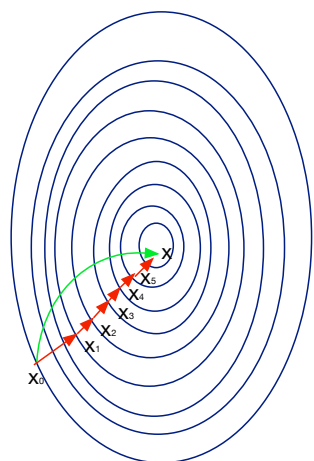


Figure 2.3 (L) A comparison of gradient descent (red) and Newton's method (green) for minimizing a function (with small step sizes).

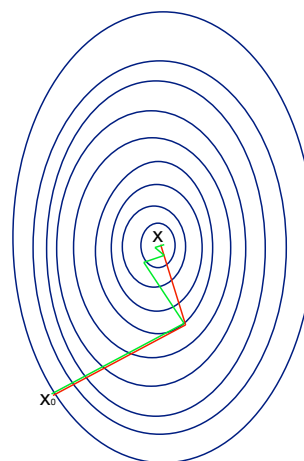


Figure 2.3 (R) A comparison of the convergence of gradient descent with optimal step size (in green) and conjugate vector (in red) for minimizing a quadratic function associated with a given linear system.

Newton's method uses curvature information to take a more direct route. Conjugate gradient, assuming exact arithmetic, converges in at most n steps where n is the size of the matrix of the system (here $n=2$ in Figure 2.3).

In this work, the CG and Quasi-Newton method were used for the calculations. To search the global minimum, the CG is more efficient when the initial geometry guess is far from the minimum, while Quasi-Newton method is seemed to be as stable as CG method, and is close to minimum much faster than CG method. What need to be aware of is that Quasi-Newton method could potentially lead to the local minimum.

2.3.1. Transition states search: Nudged Elastic Band (NEB)

The transition states were searched using Nudged Elastic Band (NEB) method [38,39].

The NEB is a method to find a minimum energy paths (MEP) between a pair of stable states. This pair of stable states is composed of an initial state (IS) and a final state (FS), which are the local minima on the whole potential energy surface (PES). Along the direction of MEP from the IS to FS, the path is supposed to pass through at least one first order saddle point, which is so-called transition state (TS).

The NEB is a chain-of-states method in which a string of images are connected together to trace out a pathway. The Figure shows the diagram of the NEB pathway and MEP pathway. The NEB path is relaxed to the MEP through a force projection scheme in which potential force act perpendicular to the band, and the spring acts along the band.

$$F_i^{NEB} = F_i^\perp + F_i^{S||} \quad (2.3.1)$$

Where the F_i^\perp is the force due to the potential perpendicular to the band, and $F_i^{S||}$ is the spring force along the band.

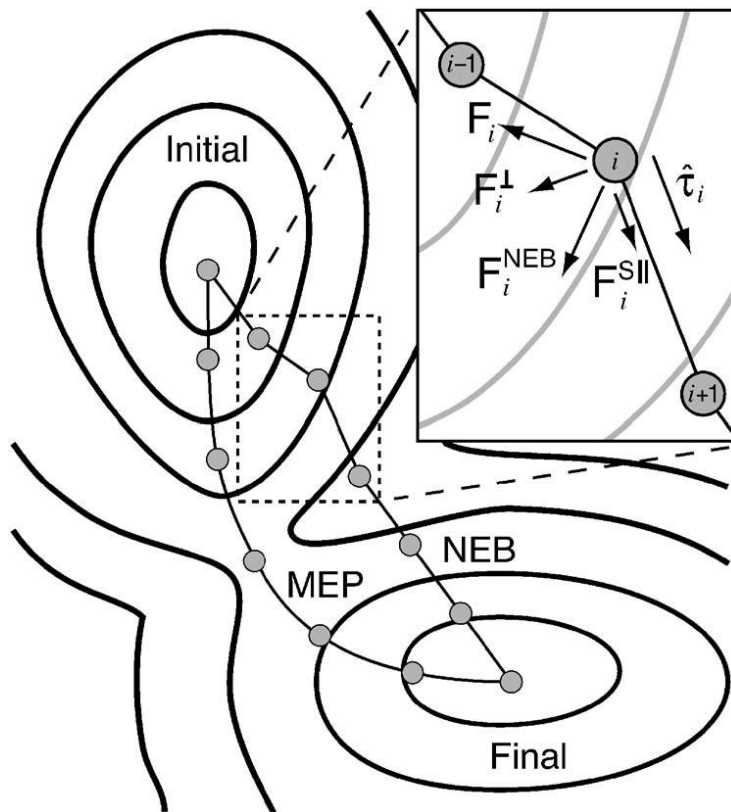


Figure 2.5 Two components make up the nudged elastic band force F_i^{NEB} : the spring force $F_i^{S||}$, along the tangent $\hat{\tau}_i$, and the perpendicular force due to the potential F_i^\perp . The unprojected force due to the potential F_i is also shown for completeness. [40]

2.4. Bader Charge Analysis

If a spatial basis set like plane-waves is used to solve the Schrodinger equation, the wave-function belongs to the whole system instead of to individual atoms. In this case, to define the boundary between different atoms is useful to study the electronic charge property. Bader uses what are called zero flux surface to divide atoms. In general, the charge density reaches a minimum between atoms and this is a natural place to separate atoms from each other.

Henkelman's Group developed a code to find the Bader Volume without lattice bias[41].

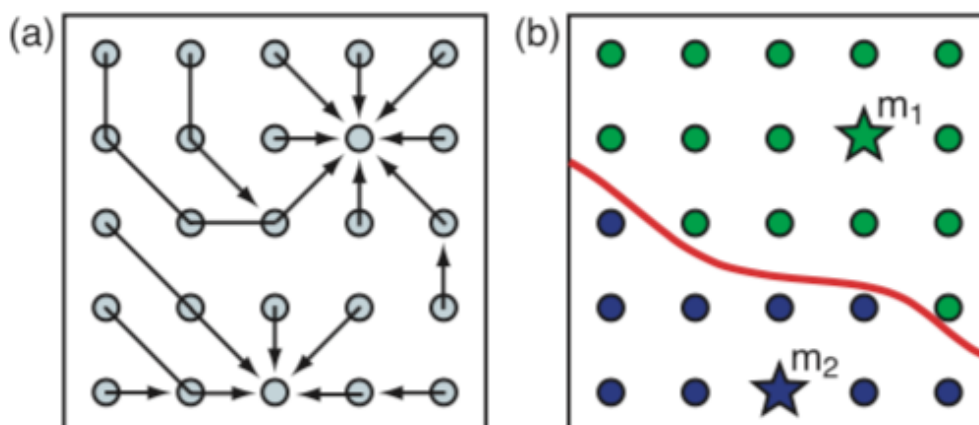


Figure 2.6 An illustration of the steepest ascent paths (a) on a charge density grid to find the Bader volumes using the on-grid analysis method. These ascent trajectories are constrained to the grid points, moving at each step to the neighboring grid point towards which the charge density gradient is maximized. Each trajectory either terminates at a new charge density maximum, m_i , or at a grid point which has already been assigned. After all grid points are assigned (b), the set of points which terminate at each maximum (green to m_1 and blue to m_2) constitute that Bader volume. The Bader surfaces (red curved line) separate the volumes. [41]

2.5. Computational details

All the spin polarized calculations were performed using Perdew-Burke-Ernzerh (PBE) generalized gradient approximation (GGA) [31] functional within the framework of density functional theory implemented in VASP code [42,43]. The projector-augmented-wave (PAW) pseudopotentials [35] were utilized to describe the valence-core interaction and a plane-wave kinetic energy cut-off of 450 was employed.

The ion step optimization using CG [36] and Quasi-Newton's Method [37], the criteria for the Hellman-Feynman force of 0.02 eV/\AA was used for optimizations.

2.6. Adsorption, activation and dissociative chemisorption energy

The adsorption energy of surface species is defined as (for the single atom adsorption use the second formula):

$$E_{ad(X)} = E_{(sur)} + E_{(X)} - E_{(X/sur)} \quad (2.5.1)$$

For the single atom adsorption:

$$E_{ad(X_2)} = E_{(sur)} + \frac{1}{2}E_{(X_2)} - E_{(X/sur)} \quad (2.5.2)$$

Where $E_{(sur)}$, $E_{(X)}$ and $E_{(X/sur)}$ are the energies of the catalyst surface, X in the gas phase and X adsorbed on the catalyst surface, respectively. The larger $E_{ad(X)}$ is the more strongly the species X binds on the surface.

The activation energy is defined as the energy barrier for the surface species dissociate to isolated atoms on the surface.

$$E_{a(X)} = E_{(X^\# / sur)} - E_{(X/sur)} \quad (2.5.3)$$

Where the $E_{(X^\ddagger/sur)}$ is the energy of the transition state, $E_{(X/sur)}$ is the chemisorption of the X specie. The higher the activation energy is, the less possible the reaction proceed to the product.

The dissociative chemisorption energy is defined as the energy deference between the dissociative species and the chemisorption species, which is

$$E_{Dis} = E_{ad(A-B)} - E_{ad(AB)} \quad (2.5.4)$$

Where $E_{ad(A-B)}$ is the dissociative species on the surface for the AB molecule.

Results & Discussions

3. NO dissociation on Ru (0001) surface

The Ruthenium metal is reported to be paramagnetic [45]. Ru bulk is closed-packed hexagonal lattice (Figure 3.1), therefore its unit cell would have two lattice parameter, and experimental lattice constants [45] are $a=2.706\text{\AA}$ $c=4.280\text{\AA}$. The Ru (0001) surface is the most common exposure surface. In this chapter, we focus on NO dissociation on Ru (0001) surface.

3.1. Ru bulk and surface optimization

For the bulk calculations, the K-mesh points used $16 \times 16 \times 10$. Fitting by the Murnaghan Equation of State [46], as shown in the Figure 3.2, to the calculated total energies at different lattice parameters, both the theoretical lattice constants and theoretical c/a ratio were tested.

As it's shown in Figure 3.1, at c/a ratio of 1.583, the theoretical lattice constant is $a=2.725\text{\AA}$, $c=4.316\text{\AA}$ which is in good agreement with experimental results. Therefore, it's used throughout this work.

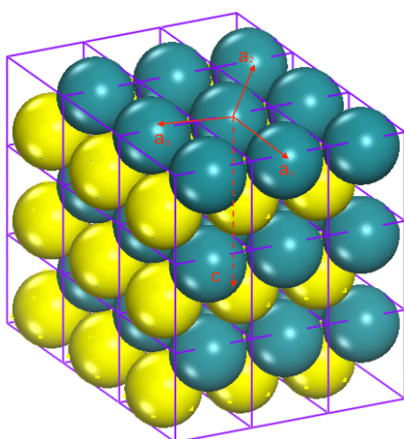


Figure 3.1 Ru lattice

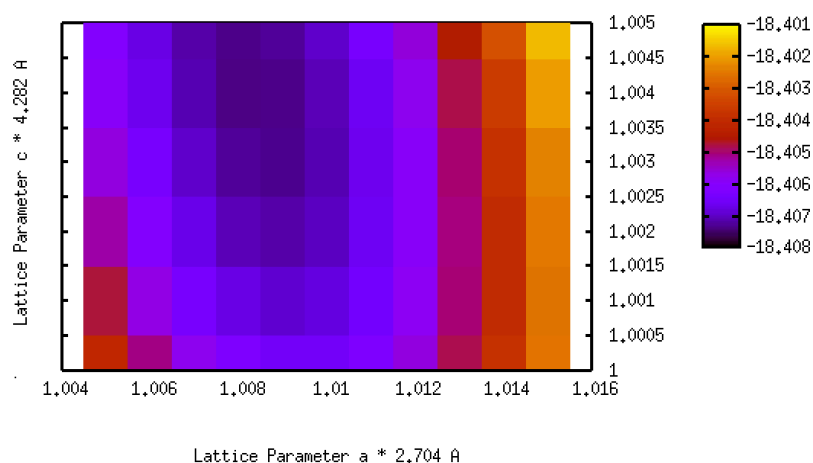


Figure 3.2 Total energy with different lattice parameter a & c fitted to Birch-Murnaghan equation of state. The energy units are eV

To model the Ru (0001) surface, the optimized bulk was cleaved along the (0001) direction. The XY unit cell needs to be large enough to avoid the interaction between the adsorbates along the XY plane. To eliminate the interaction along the Z axis between the slabs, the slabs are separated by about 15\AA of vacuum. The cleaved Ru (0001) used a $p(3 \times 3)$ surface unit with a $6 \times 6 \times 1$ K-point mesh in the calculations. The number of layers were tested from 4 to 6 and, their adsorption energies of NO difference are around 0.1-0.2eV but the trend is the same. To study the surface properties and

reactivity on the surface, it may be more reasonable to have more layers to get a better description of the system. However, using more layers mean that it's more computationally demanding. After careful tests, the adsorption energy and activation energy differ slightly between 5-layer slab model and 6-layer's. Thus, in this work, 5-layer slab was used to study the surface properties and NO dissociation.

A 3x3 supercell (see figure 3.3(a)) has been used, which mean that the length of a_1 and a_2 lattice vectors are three times as large as the primitive cell. The three bottom layers were fixed, and all other atoms are fully relaxed. For the optimized Ru (0001) surface, the interlayer distances range from 2.093 Å to 2.158 Å. The topmost Ru interlayer spacing of the optimized Ru (0001) surface is contracted by 3.0%, that is close to LEED spectroscopy values of 2.1% [47], while the spacing between second and third layers change slightly.

There are several adsorption sites which are top sites, bridge sites, and hollow sites, as shown in Figure 3.2 (a). Since the Ruthenium is hexagonal close packing, where the layers are alternated in the ABAB... sequence, as shown in Figure 3.2 (b). Consequently, there are two hollow site on the Ru (0001) surface --- HCP (hexagonal close packing) sites and FCC (face centered cubic) site.

The spin density distribution of Ru (0001) surface was studied. As shown in the Figure 3.2 (c), the spin density is near to zero, and the total magnetic moment of the surface system is close to zero, which is in agreement with its paramagnetic property.

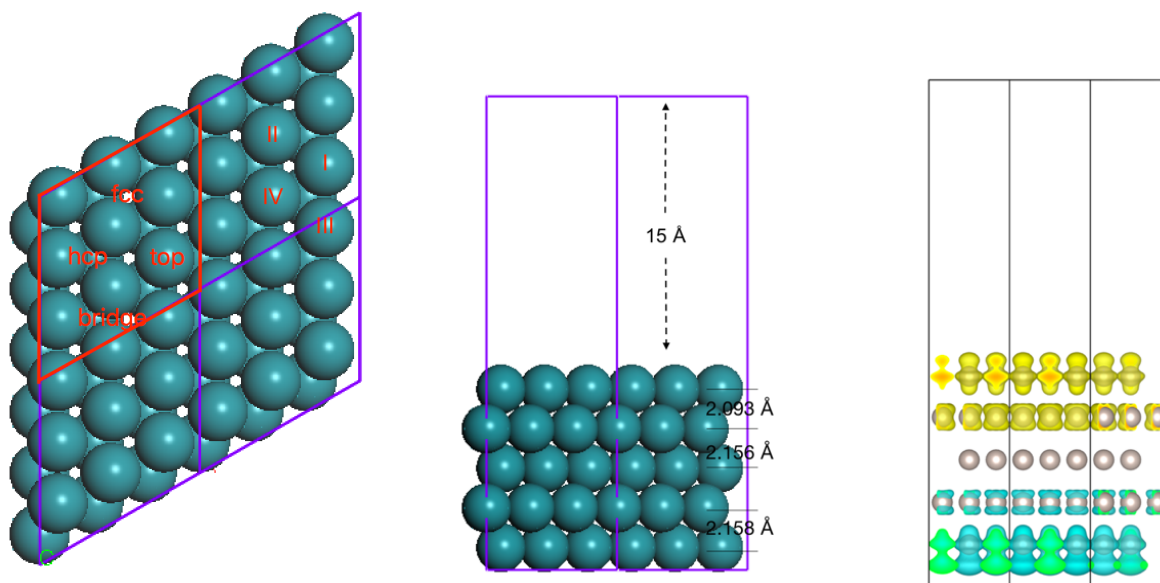


Figure 3.3 Ru (0001) surface top view(a), side view (b), Spin density distribution (c). The yellow color is spin up, and blue on is spin down. The volume of the spin charge density is at 10^{-4} order

The same approach was used to model other surface: step surface $(10\bar{1}5)$, step surface $(10\bar{1}9)$, saw step surface $(11\bar{1}5)$, surface $(10\bar{1}9)$ surface $(10\bar{1}0)$, that will be shown in the following chapter.

3.2. Molecular adsorption of NO

3.2.1. Adsorption energies and geometries

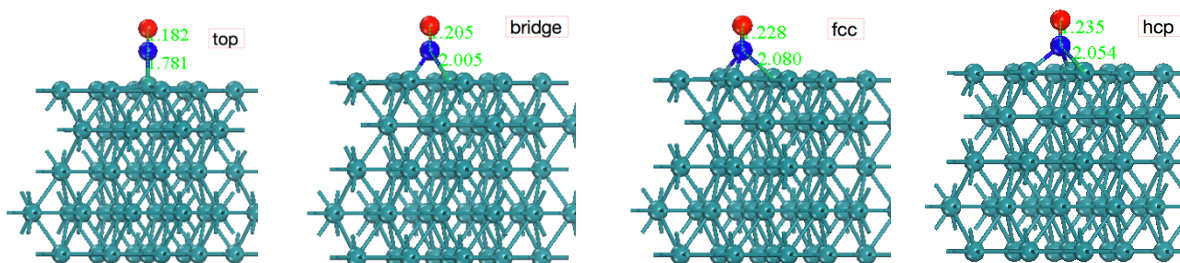


Fig.3.4. top adsorption(a), bridge adsorption(b), FCC adsorption(c), HCP adsorption(d)

The molecular chemisorption of NO on the Ru (0001) surface has been investigated. After careful studies, the NO molecule is not able to parallel adsorb on the Ru surface remaining a molecular state and all the NO adsorbed molecules are perpendicular to the surface. There are four representative adsorption sites on Ru (0001) surface, top site, bridge site, FCC site and HCP site, as shown in Figure 3.4 (top view was shown in Fig.3.3). The Ru-N bond length and N-O bond length are shown in the given figures.

Table 3.5 Calculation results and literature data for the NO chemisorption energy

Functional	This Work	B.Hammer [48,49]			M.Gajdos[50,51]	
	PBE	PW91	PBE	RPBE	PW91	RPBE
Top	-2.45	-2.14	-2.06	-1.75	-2.51	-2.19
Bridge	-2.43	-2.40	-2.32	-1.94	-2.38	-1.91
FCC	-2.36	-2.49	-2.40	-2.01	-2.38	-2.00
HCP	-2.68	-2.73	-2.64	-2.24	-2.59	-2.21

As listed in Table 3.5, the PW91 and PBE functional give very close results. Compared to PW91 and PBE, the RPBE shows a considerable destabilization as expected. In our work, all the calculations were performed under PBE level. All the results confirm that the NO molecule prefer to adsorb on hcp site, and the adsorption energy is about -2.68 eV. According to B.Hammer's results, the adsorption preference order is hcp > fcc > bridge > top, while our results and M. Gajos's results agree that hcp > top > fcc ≈ bridge. That could attribute to the same reason to the single atom adsorption. To rationalize the adsorption results, the Bader charge analysis were performed.

3.2.1. Bader Charge Analysis

The charge transfer of chemisorption of NO was also investigated. The Bader charge analysis shows that the N in adsorbed NO over Ru surface possessed more negative charges than the N in NO molecule by range 0.40e to 0.66e depending on the adsorption sites. The electrons mostly come from the adsorption site atoms and a few from the atoms near adsorption sites.

The more detailed data for charge transfer is shown in Table 3.6.

Table 3.6 Charge Transfer

	Top	Bridge	FCC	HCP
N	0.340	0.489	0.518	0.661
O	-0.070	0.006	0.067	-0.022
Ru-I	-0.299	-0.199	-0.201	-0.205
Ru-II	-0.008	-0.050	-0.157	-0.035
Ru-III	-0.010	-0.058	-0.003	-0.180
Ru-IV	-0.019	-0.181	-0.184	-0.182

*The positive mean gain electrons, negative mean lose electrons. The labels of Ru are shown in Figure 3.3

In general, in the hcp adsorption site, the NO molecule attract more electrons from the binding Ru atoms. The NO molecule also gains some electrons from the oxygen atom by 0.022 e. That indicates the electronic density between N and Ru surface is more condensed, which means the Ru-N bond would be more stable, leading to a relatively lower adsorption energy. For the top site adsorption, the the binding NO will attract more electrons from the Ru atoms by about 0.3 e, same as the HCP adsorption, it also gains 0.070 e from the oxygen atom. The bridge site and fcc site, the surface Ru atoms lose about 0.5 e to the NO molecule, while oxygen, unlike in hcp and top site, will possess more electrons about 0.006-0.067 e. Interestingly, when the charge transfers are closed, the adsorption energies are also closed.

3.3. Atomic adsorption and diffusion of N and O

3.3.1. Atomic adsorption

We investigated the atomic chemisorption of nitrogen and oxygen. The results for the adsorption energy and Ru-O bond lengths are listed in Table 3.1, The corresponding geometries could be found in Figure 3.3. the bond length of Ru-N bond is about 1.67Å to 1.94Å, which is quite close to B.Hammer's results ($\Theta = \frac{1}{6}$) except for the top site adsorption. The atomic nitrogen can strongly bind in HCP site with a high adsorption energy of -1.06 eV, while the other sites are far less favorable than most stable adsorption site. For the top site, the N atom possesses a positive adsorption energy of 0.95 eV, meaning that it tends to desorb from the surface instead of binding with Ru atom. The bridge site also shows a tiny adsorption energy of -0.08 eV.

At low coverage of $\Theta = \frac{1}{9}$ monolayers for the atomic species, both atomic N and O strongly adsorb on the Ru (0001) surface, and prefer to adsorb on HCP 3-fold sites. The results show that the adsorption site preference order: HCP > FCC > bridge > top. Compared to the Hammer's result [48,49], which is done in DACAPO code, we note that the adsorption energies differ quite significantly, especially for the N atomic adsorption. M. Gajods's results [50,51], conducted in VASP code, show very close results to ours. M. Gajods suggest the differences come from some sensitive parameters determining basis-set and k-point convergence between VASP and DACAPO calculation. [50,51]

Table 3.1 Calculation results and literature data for the atomic chemisorption energy (eV) of nitrogen and oxygen and Ru-N(O) bond lengths (Å) given in parentheses

	This work		B.Hammer [48,49]		M.Gajdos [50,51]	
	N	O	N	O	N	O
Top	0.95(1.67)	-1.44(1.76)	0.32(1.96)	-1.51(2.06)	-	-
Bridge	-0.08(1.87)	-2.18(1.96)	0.34(1.93)	-1.66(2.03)	-	-
FCC	-0.32(1.94)	-2.50(2.05)	0.04(2.02)	-1.99(2.11)	-	-
HCP	-1.06(1.93)	-2.90(2.01)	-0.45(1.98)	-2.16(2.07)	-0.94	-2.67

The calculated Ru-O bond length at HCP site is 2.01 Å, which is quite close to the LEED-determined value of 2.03 Å [52]. For the oxygen atomic adsorption, the oxygen also prefers to adsorb on HCP site. In contrast to the nitrogen, the oxygen can also strongly bind with Ru on other sites with a higher binding energy of -1.44 eV for top site, -2.18 eV for bridge site and -2.50 eV for FCC site.

Compared to B.Hammer's results, the atomic adsorption from DACAPO seemed to underestimate the binding energy, while M.Gajos' result show very good agreement with ours. C. Stampfl's [53] results give the same adsorption preference, while the most favorable adsorption site (HCP) binding energy is about -2.65 eV at coverage of 1/4 monolayers. Even though the coverage is higher than Hammer's work, the adsorption is still lower than -2.16 eV. Thus, we believe our results are reliable.

3.3.1. Atomic species diffusion

As shown above, the most favorable adsorption site is HCP site, and the second one is FCC site, which are more stable than rest of adsorption sites. For atomic diffusion, we will only consider the configuration between high symmetry threefold sites. The transition state of the diffusion from HCP site to FCC site can be approximated as the bridge site adsorption. Those results are very close to the results from NEB method, while much less computational demanding. The energy profiles for the atomic diffusion are shown in Figure 3.4

As the results shown, it is found that the N atoms bind most strongly in the threefold hollow site. The HCP sites have 0.75eV preference than FCC sites. The N bridge adsorption site could be considered as transition state between HCP and FCC sites. The process has an energy barrier of 0.23eV from FCC to HCP site (or 0.98eV from HCP site to FCC site).

Similarly, the oxygen adsorption and diffusion has been studied using same approach. The adsorption preference is same as that for nitrogen. HCP site adsorption is 0.4eV lower than FCC site. The process from FCC site diffusing to HCP site has a 0.32eV energy barrier. Reversely, it has to overcome an energy barrier of 0.72eV from HCP site to FCC site for oxygen atom diffusion.

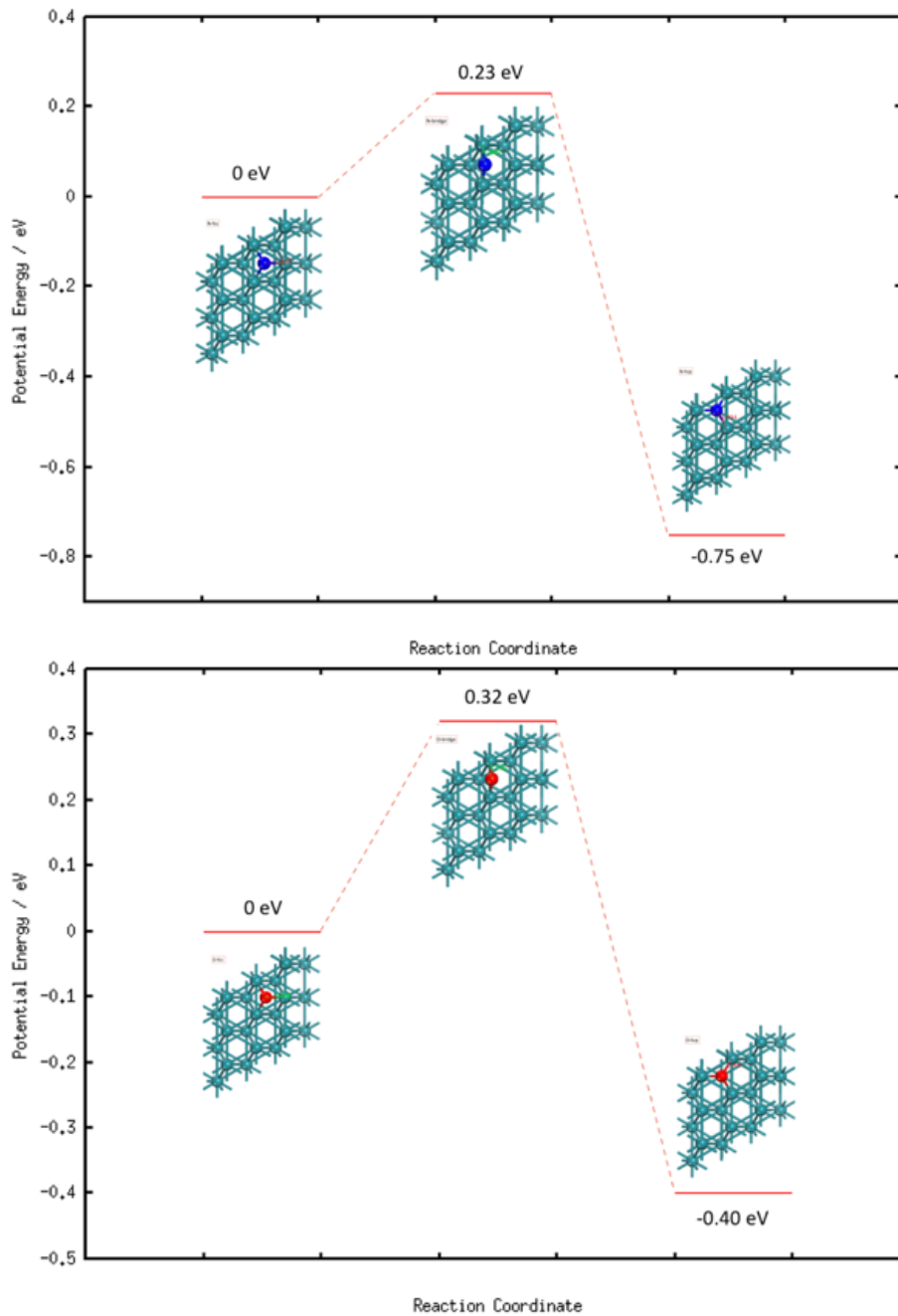


Figure 3.4 Single atom diffusion between threefold sites, for N atom (up), and O atom (down)

Consequently, if there is an atomic species of nitrogen or oxygen, it will easily diffuse to the more energetic stable HCP site, since the FCC to HCP forward energy barriers are as low as about 0.2-0.3 eV, while the backward energy barriers are more than 0.7-0.9 eV.

3.4. N and O Co-adsorption.

In this part, the double atoms adsorption corresponding to N_2 , O_2 and NO have been studied. For the reaction $NO = 1/2 O_2 + 1/2 N_2$, studying the dissociated adsorption gives us information about difficulties in N_2 and O_2 desorption.

In a 3×3 slab, several configurations for N and N, O and O and N and O were studied:

for double N and O atoms co-adsorption: N(O) hcp + N(O) hcp, N(O) hcp + N(O) fcc; as for the the configuration for N and O co-adsorption, N hcp + O hcp, N hcp + O fcc, N fcc + O hcp and N fcc + O fcc were studied.

The interaction energy here is defined as the interaction between two adsorbed atoms with respect to infinite distance, which is calculated by following formula:

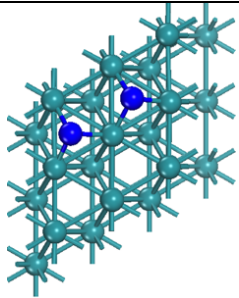
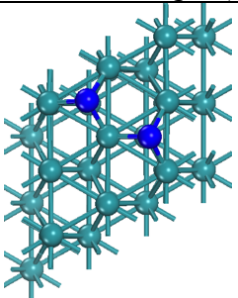
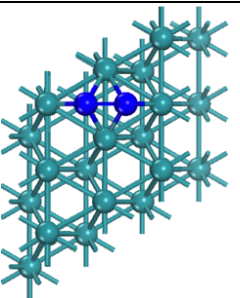
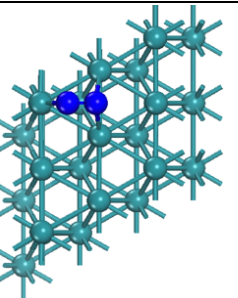
$$E_{int} = E_{AB}^{AB} - E_A^A - E_B^B$$

Where E_{int} is the interaction energy between atomic species, E_{AB}^{AB} is the energy of AB specie adsorbed A and B site respectively, E_A^A is only A specie adsorb on A site; E_B^B is only B specie adsorb on B site.

3.3.1 N-N Co-adsorption

The geometries of co-adsorption of nitrogen atoms are given in the Table 3.2. The bond length of Ru-N is about 1.91Å-2.0Å. Compared to the Ru-N bond length in single atomic adsorption, the bond length changes slightly. For the FCC-FCC co-adsorption, the bond length almost remains the same. The bond close to adjacent atom is 0.05Å longer than the bond length in single atomic adsorption, while the rest of the bond lengths decrease about 0.01 Å. That comes from the weak interaction (0.18 eV) between two nitrogen atoms. The atomic adsorption energy of two nitrogen, with respect to N_2 in gas phase and bare Ru (0001) surface, are -0.45 eV. The separated adsorption of two atomic nitrogen leads to -0.64 eV. It shows a modest repulsion between two nitrogen atoms.

Table 3.2 The calculated N-N coadsorption geometries, adsorption energies (eV) and bond length (Å)

Geometry				
	N(fcc)-N(fcc)	N(hcp)-N(hcp)	N(hcp)-N(fcc)	N(hcp)-N(bridge)
E_{ad} (eV)	-0.45	-1.66	0.90	0.01
E_{int} (eV)	0.18	0.46	2.33	1.15
Ru-N bond (Å)	1.93 1.93 1.99	1.91 1.94 1.97	1.99 2.00 2.00	1.96
Ru-N bond (Å)	1.99 1.93 1.93	1.97 1.94 1.91	2.14 2.14 1.99	2.34 2.34
R_{N-N} (Å)	2.96	2.98	1.70	1.12

Compared to FCC-FCC co-adsorption, the HCP-HCP co-adsorption shows very similar trend, but a lower adsorption energy and higher interaction energies. The nitrogen atoms strongly bind with the Ru at HCP sites with adsorption energy of -1.66 eV. Due to the repulsion between the two nitrogen atoms (0.46 eV), the bonds close to the adjacent atoms are prolonged, while the rest of the bonds are slightly shortened.

When one nitrogen atom adsorbs on Hcp site and the other one on fcc site, this configuration possesses a positive adsorption energy of 0.90 eV, which indicates the nitrogen can hardly attach to the Ru (0001) surface. The strong repulsion between two atoms are as high as 2.33 eV. Interestingly, when the molecule nitrogen adsorbs on the hcp and bridge sites, the N-N bond is slightly activated

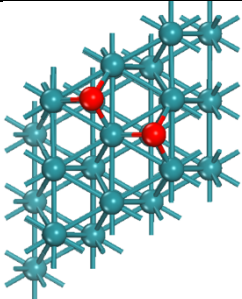
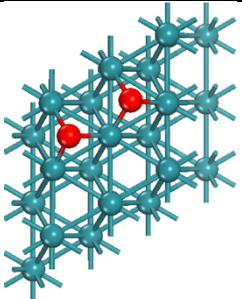
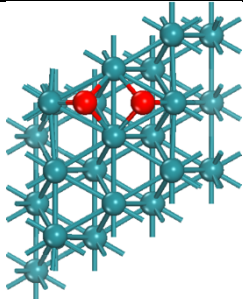
with a prolonged bond length of 1.12 Å. It shows a tiny adsorption energy of 0.01 eV, that could be considered as a molecular adsorption of nitrogen.

The co-adsorption of two nitrogen atoms suggests that nitrogen can strongly bind with Ru at both HCP site. The FCC-FCC site, the adsorption energies is much lower than HCP-HCP site. The other two configurations indicate that the surface atomic nitrogen species have great potential to desorb from the surface. That was confirmed by N_2 recombination results, which could provide a favorable desorption channel[55].

3.3.2 O-O Co-adsorption

The chemisorption of two atomic oxygen is considered in the following. Bond lengths and chemisorption energies for FCC-FCC, HCP-HCP and HCP-FCC configurations are given in the Table 3.3.

Table 3.3 The calculated O-O coadsorption geometries, adsorption energies (eV) and bond length (Å)

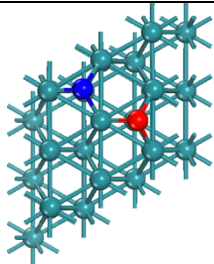
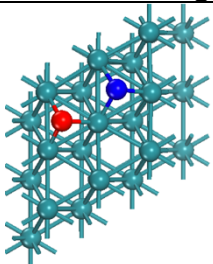
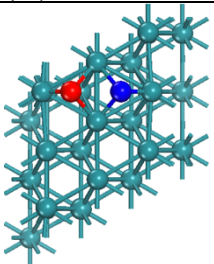
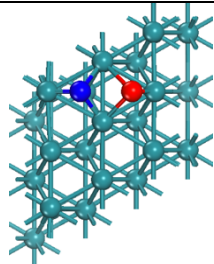
Geometry			
	O(hcp)-O(hcp)	O(fcc)-O(fcc)	O(hcp)-O(fcc)
E_{ad}	-5.52	-4.87	-4.12
E_{int}	0.28	0.14	1.28
Ru-O bond	1.99 2.01 2.05	2.04 2.02 2.07	1.89 2.09 2.09
Ru-O bond	2.05 2.01 1.99	2.04 2.06 2.02	2.18 2.18 1.89
R_{O-O}	2.92	2.92	2.34

The bond length is about 1.89-2.07Å. Not surprisingly, the adsorptions are quite strong for the oxygen, even for the HCP-FCC site is as low as -4.12 eV. Similar to double nitrogen atoms co-adsorption, the bond lengths of Ru-O change slightly due to the repulsion between oxygen atoms. However, compared to N-N atoms interaction energies, the repulsion between oxygen is smaller, especially the HCP-FCC configuration. Unlike the N-N (HCP-FCC) adsorption, the oxygen adsorbing on HCP-FCC site tend to be more separated. As shown in N-N (HCP-FCC) configuration, the N-N distance is as close as 1.70Å, where N-N bond is nearly formed, while the O-O distance is about 2.34Å. Consequently, the interaction between two oxygen atoms are less significant, leading to a more stable adsorption state.

The results suggest that the dissociated O_2 can strongly bind with the Ru atoms at threefold sites. For the re-combinative O_2 desorption, however, the adsorption is so stable, meaning that this process is so endothermic, that oxygen will remain at the surface.

3.3.3 N-O Co-adsorption

Table 3.4 The calculated N-O coadsorption geometries, adsorption energies (eV) and bond length (Å)

Geometry				
	N(hcp)+O(hcp)	N(fcc)+O(fcc)	N(fcc)+O(hcp)	N(hcp)+O(fcc)
E_{ad}	-4.56	-3.61	-2.78	-3.08
E_{int}	0.36	0.16	1.39	1.44
Ru-N bond	1.92 1.93 1.97	1.91 1.99 1.91	2.03 2.03 1.83	1.86 1.97 1.97
Ru-O bond	2.05 2.01 1.99	2.03 2.03 2.07	1.89 2.14 2.14	2.41 2.41 1.84
R_{N-O}	2.95	2.95	2.32	2.43

The configurations for N and O co-adsorption were studied, as shown in Table 3.4: N(hcp)+O(hcp), N(fcc)+O(fcc), N(fcc)+O(hcp) and N(hcp)+O(fcc). In the 3×3 slab, the most stable configuration, not surprisingly, is the N(hcp)+O(hcp), since the atomic nitrogen and oxygen prefer to adsorb on hcp sites. The adsorption energy is -4.56 eV. The separated adsorption energy of atomic N and O leads to -4.92 eV. The HCP-HCP possesses much lower adsorption energy than other configurations about 0.95-1.78 eV. Since the diffusion energies from fcc site to hcp site for N and O atoms are just about 0.2-0.3 eV, the other configurations have great potential to transfer to more energetic stable structure, especially for the hcp-fcc sites which have about 1.40 eV interaction between N atom and O atom. Based on this fact, for the NO decomposition, we only consider the hcp-hcp adsorption.

3.5. NO dissociation

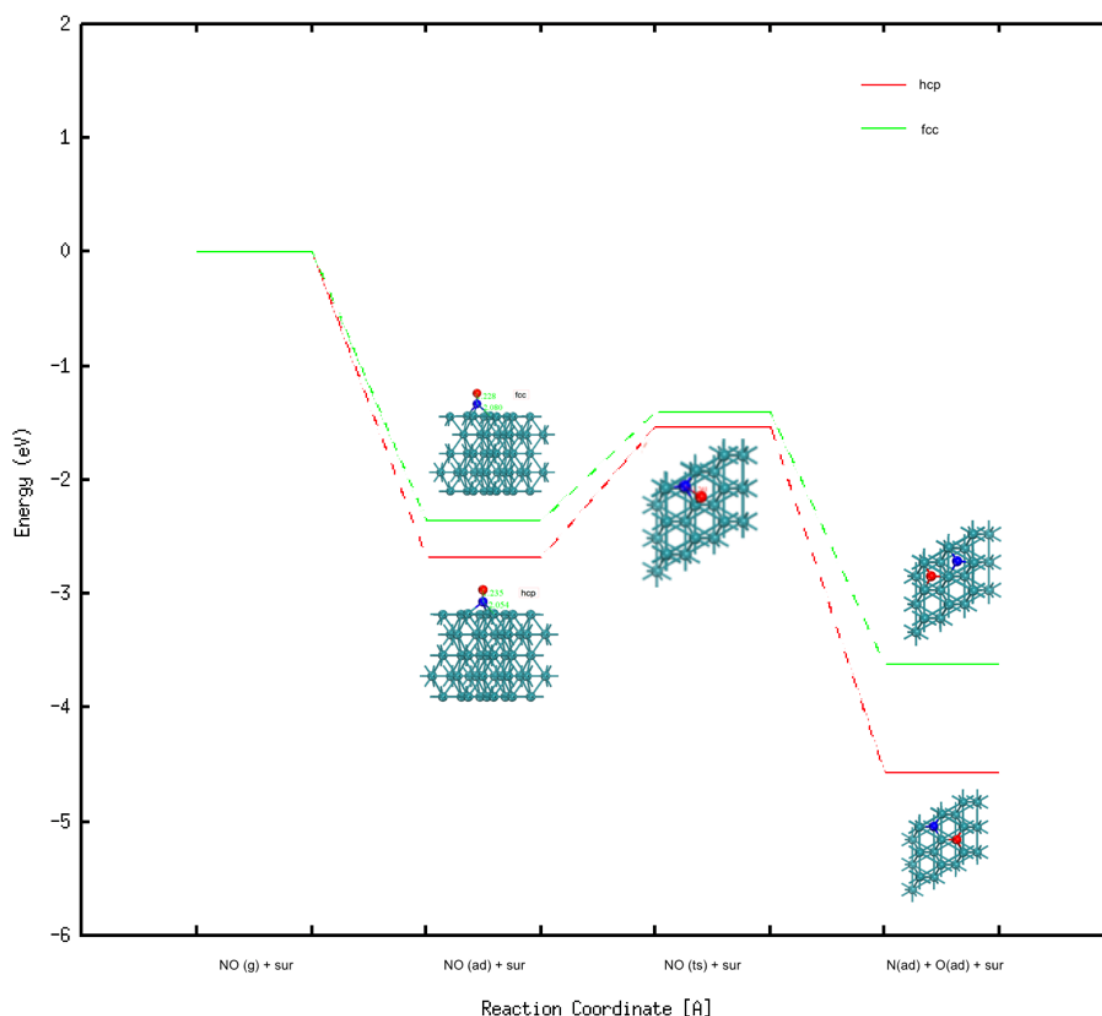


Figure 3.9 Energy profile of NO dissociation on Ru (0001) surface for hcp and fcc rutine

Table 3.7. Energy barrier and dissociation energy of NO dissociation of Flat Ru(0001) for hcp and fcc sites

Reaction rutine	hcp	fcc
NO(ad)+sur	-2.68	-2.36
NO(ts)+sur	-2.58	-1.40
N(ad)+O(ad)+sur	-4.14	-3.61
$E_{activation}$	1.17	0.96
$E_{Dissociation}$	-1.80	-1.25

To study the NO dissociation on Ru (0001) surface, only the two most energetically stable adsorption sites, fcc-fcc and hcp-hcp, were studied. The energy profiles are shown in Figure 3.9, and the related energies are listed in Table 3.7. The figure includes the relative energy with the NO in gas phase and surface as zero energy reference, the adsorption state of NO, the transition state of NO dissociation, and the dissociative atomic N and O atoms.

Figure 3.9 shows the calculated minimum energy path (MEP), and indicates that NO dissociation is more thermodynamically favorable than molecular desorption. The calculated energy barrier is quite

close to B.Hammer's results using different approach to find transition states. For the NO adsorb on hcp site, the energy barrier for NO dissociation is about 1.17 eV, and on fcc site, it has a slightly lower energy barrier of 0.96 eV. However, since the NO tend to adsorb on the hcp site instead of fcc site, and the dissociative atomic oxygen and nitrogen are more energetic favorable on both hcp site, but not on fcc site. Thus, pathway of hcp routine is more favorable than fcc routine, especially when the reaction occurs in realistic environment in three-way catalyst where the temperature can be up to 1000 K.

4. Step Effect

Steps are generally found to possess better reactivity than terraces [48,49,55,56]. Using scanning tunneling microscope (STM), it has been found that the NO prefer to dissociates at steps on a Ru(0001) surface[56]. B.Hammer investigated NO bond activation at a corrugated Ru (0001) surface using Density functional theory. Monatomic steps in the Ru surface are found to offer completely new reaction pathways with highly reduced energy barriers compared to reaction at a flat surface. B. Hammer suggest that the step as active center, lead to a much lower energy barrier for NO dissociation. The presence of the step, and low-coordinated Ru atoms are claimed to be the reason for such extraordinary reactivity for the NO dissociation. However, B.Hammer's model may be not able to describe the step correctly. In the following part, we propose an improvement for the NO dissociation on the step and the new understanding of this issue.

4.1. Step model

To model the steps, we take a supercell with double steps, where the terraces are consisted of Ru (0001) surface. In this work, the stepped Ru surface of $(10\bar{1}5)$ and $(10\bar{1}9)$ were studied. Since the Ru surface of $(10\bar{1}5)$ and $(10\bar{1}9)$ are quite similar to each other, except the number of atoms in terrace. The terrace in Ru $(10\bar{1}9)$ is composed of 4 atoms, while $(10\bar{1}5)$ is 2 atoms. For the step site, the reactivity properties of these two surfaces are almost identical that NO adsorption energies, dissociation barriers are very closed. We first investigate the NO reactivity on step Ru $(10\bar{1}5)$ surface.

To describe Ru $(10\bar{1}5)$ surface, the 2x super-cell was used for this study. In the 2x super-cell, the k-mesh points of $1\times 2\times 1$, $2\times 4\times 1$, $3\times 6\times 1$, $4\times 8\times 1$ were tested, and the total energy are listed in the Table 4.1. In this work, the k-mesh points of $3\times 6\times 1$ is used in all 2x super-cell calculation since, there is only energy difference of 0.006eV between $3\times 6\times 1$ and $4\times 8\times 1$, which is not significant. However, the k-mesh point of $4\times 8\times 1$ is more than twice computational cost compared with $3\times 6\times 1$. The vacuum region has been used between repeated cells in the z-direction. The vacuum is 15Å thick which is large enough to prevent the interaction between slabs, Same approach was used to calculate the Ru $(10\bar{1}9)$ surface.

Table 4.1 Total energy and computing time obtained with different K-Points

K-Points	Energy (eV)	Time (s)
$1\times 2\times 1$	-417.51286	23260
$2\times 4\times 1$	-415.92264	26071
$3\times 6\times 1$	-415.75986	47946
$4\times 8\times 1$	-415.75343	80187

The calculations were done using 12 processors

For the Ru ($10\bar{1}5$) surface, there are two types of steps: first steps are composed of four atoms; the other steps are composed of three atoms, as shown in Figure 4.1 below (Yellow atoms).

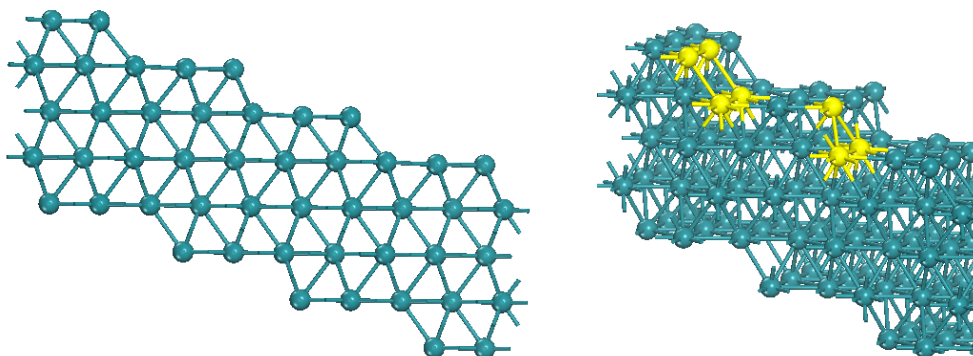


Figure 4.1 Surface ($10\bar{1}5$) side view

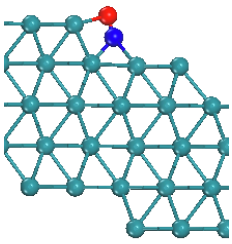
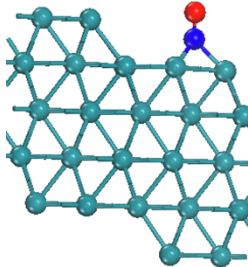
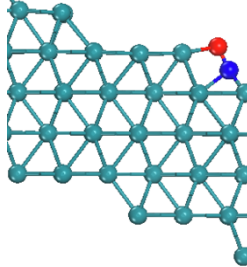
4.2. Adsorption of Molecular NO.

The adsorptions of NO molecule were calculated in 2x supercell for two stepped surface as shown in Table 4.2. There are several types of NO adsorption. Here all the NO adsorption geometries are HCP site, since HCP sites were found to be most stable also near step sites.

When the molecular NO adsorbs on the fourfold step, this configuration is most energetic favorable, whose adsorption energy is about -2.95 eV. The NO adsorption near threefold step, possesses a binding energy of -2.53 eV, which is 0.42 eV less favorable than at fourfold step. In addition, the adsorption on the terrace is less stable than at the fourfold step.

The bond length of N-O at fourfold step is about 1.393 Å, which is slightly longer than N-O bond in terrace configuration (1.232 Å), and very close to the threefold configuration (1.373 Å). To explain this, the reason could mainly attribute that the NO molecule adsorb on the fourfold or threefold site, the O atom also coordinates with two Ru atoms at nearly bridge site, leading to activation of N-O bond.

Table 4.2 The calculated geometry and binding energy (eV) of NO adsorption on Ru ($10\bar{1}5$) surface

Geometry			
E_{ad}	Hcp at fourfold step -2.95	Hcp at terrace -2.42	HCP at threefold step -2.53

4.3. Atomic Adsorption

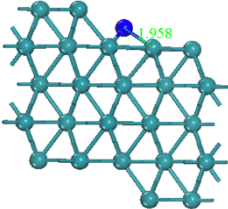
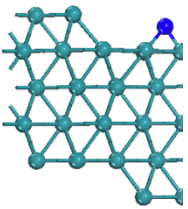
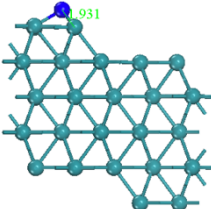
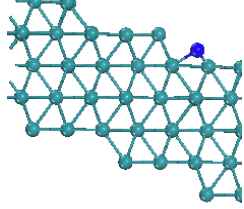
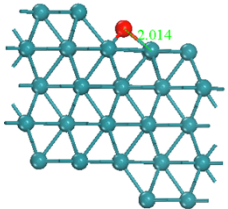
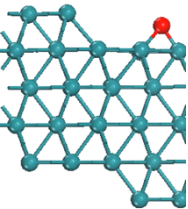
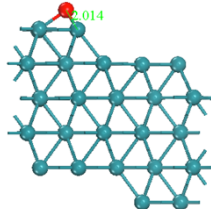
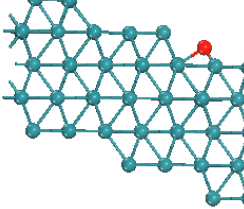
The adsorption energy of surface species is also defined as:

$$E_{ad(X)} = E_{(X-sur)} - E_{(sur)} - \frac{1}{2}E_{(X_2)}$$

Where $E_{(sur)}$, $E_{(X_2)}$ and $E_{(X-sur)}$ are the energies of the catalyst surface, X in the gas phase and X adsorbed on the catalyst surface, respectively. The larger $E_{ad(X)}$ is the more strongly the species X binds on the surface.

The atomic chemisorption of nitrogen and oxygen have been investigated, as shown in Table 4.3. The interaction of atomic species with the step surface has been considered for several different hollow sites. The top site and bridge site haven't been taken into account, since previous studies suggest that the atomic species are more likely adsorb on the hollow sites. The results for atomic adsorption configurations are listed in the Table 4.3. All the adsorption sites are on HCP site.

Table 4.3 The calculated geometry and binding energy (eV) of atomic adsorption on Ru (10 $\bar{1}$ 5) surface

Ad Site	Fourfold step	Threefold Upper	Fourfold Upper	Threefold step
Geometry				
E_{ad}	-0.60	-0.55	-0.95	-0.44
Geometry				
E_{ad}	-2.48	-2.52	-2.94	-2.34

In general, as same on the flat Ru (0001) surface, the atomic species prefer to adsorb on hcp site rather than on fcc site. The most stable adsorption site for both oxygen and nitrogen is upper terrace hcp site. Above all, their adsorption energies are close to that on flat surface, where are about -0.95 eV (N atom) and -2.94 eV (O atom), respectively. The binding energies for the rest of configurations are less stable than upper terrace hcp site.

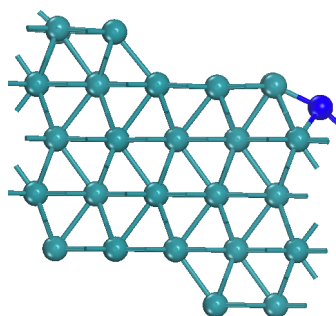


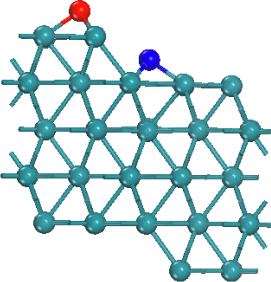
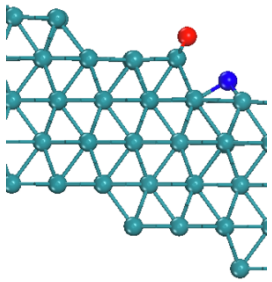
Figure 4.2 Atomic adsorption of N on step fcc site

For the N atomic adsorption, the adsorbed N atom doesn't, as strongly as O atom, bind with the Ru surface. For the hollow sites near the step, the N atom weakly adsorbs on the fcc site. According to the geometry as shown in Figure 4.2, the nitrogen atom binds with more Ru atoms than other configurations, which make this atom stay in the mid of those atoms, making the adsorption energy is as low as -0.24 eV. The binding energy is higher when the N atom adsorb near the step on hcp site. N adsorption near fourfold step is 0.16 eV more favorable than N adsorption near threefold site. Compared to N atomic adsorption, as expected, the O adsorption energies are much higher than N atoms' adsorption energies. The O atom adsorption preference and trend are quite similar to N atom. The adsorption preference order is: upper terrace > fourfold hcp > threefold hcp > threefold fcc.

It experimentally [56] found that there are significantly more N and O atoms at upper terrace near threefold steps than those at fourfold steps, that is in good agreement of our adsorption results. In addition, it also found that N atoms can also be recombined forming N_2 and desorb from the surface. Since the strong interaction between O and Ru surface, especially the upper terrace adsorption, if the O atoms are present at the step, the adsorption of further species adsorption is blocked.

4.4. N and O co-adsorption

Table 4.3 The calculated geometry and binding energy (eV) of N-O coadsorption on Ru (10 $\bar{1}5$) surface

Geometry		
E_{ad} (eV)	-4.47	-4.51

The possible final states for dissociated NO on the step (10 $\bar{1}5$) surface have been investigated by studying co-adsorption of O atom at upper terrace and N atom near step, which are the most stable configurations for the NO adsorption on fourfold and threefold step sites, as shown in Table 4.3. For the final state threefold step dissociation, we posed the separated O and N atoms on both threefold site, N atom on the hcp site near the step and O atom on the upper threefold fcc site. Interestingly, after optimization, the dissociated O atom prefers to adsorb on the bridge site instead of on its corresponding upper terrace threefold fcc site, since previous flat results show that the O can also strongly interact with bridge atoms. Moreover, the bridge site on the edge is less coordinated, leading to a more stable structure for the O adsorption.

4.5. NO dissociation on Ru step

The consideration of the initial geometries was due to the fact that these initial states are energetically favorable. As for their corresponding final states, the configurations were tested to get the most stable structure, where the initials guesses are given in both atoms on threefold site. After the geometry optimization, the dissociated NO near the fourfold site can remain a similar configuration, while the O near the threefold site prefer to stay in the bridge site on the edge Ru atoms as previous discussed. Two step dissociation routines were calculated to be the most favorable

path for the NO dissociation, as shown in Figure 4.3. The energy barriers and dissociation energies are listed in Table 4.4

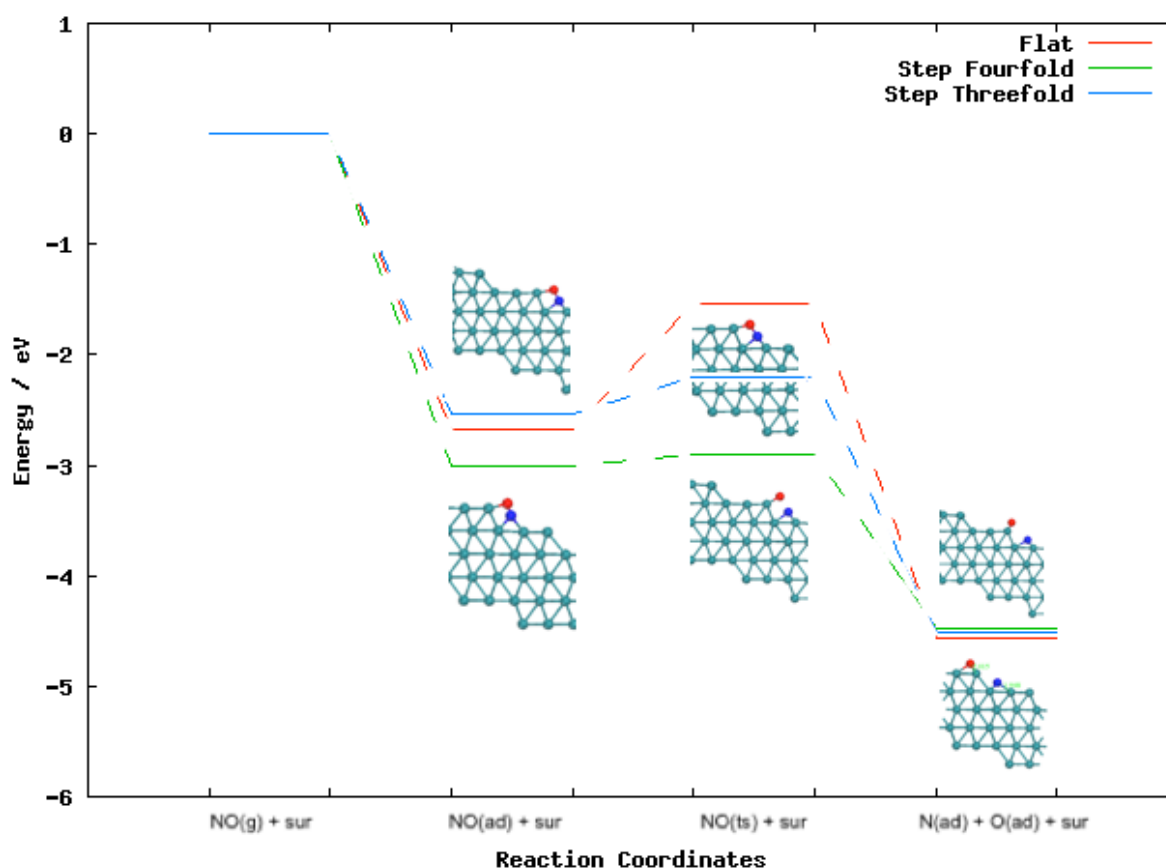


Figure 4.3 Energy profile of NO dissociation process of flat, step fourfold, step threefold pathways.

Table 4.4. Energy barrier and dissociation energy of NO dissociation of Flat Ru(0001) and Step (1015) Surface

Reaction pathways	Flat	Fourfold Step	Threefold Step
NO(ad)+sur	-2.68	-3.01	-2.53
NO(ts)+sur	-1.53	-2.91	-2.45
N(ad)+O(ad)+sur	-4.56	-4.47	-4.51
Dissociation Barrier	1.17	0.10	0.08
Dissociation Energy	-1.80	-1.46	-1.98

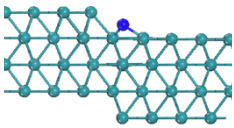
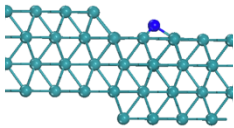
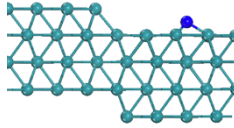
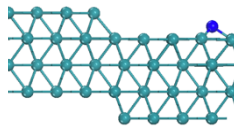
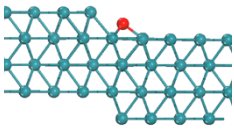
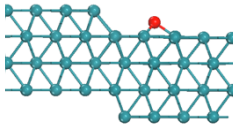
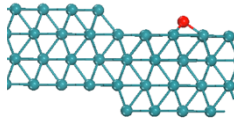
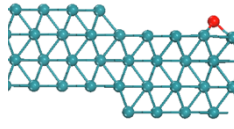
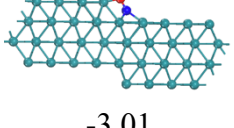
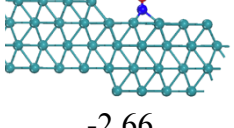
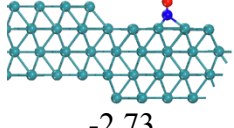
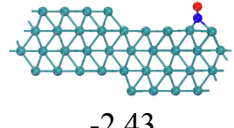
For the dissociation of NO molecule on the step site, there are two tiny energy barriers of 0.08 eV on threefold step and 0.1 eV on fourfold step. That was contributed by the unique adsorption geometry of NO molecule on the step site, where the edge Ru atoms can form a bridge bond for the O atom, leading to a relatively longer N-O bond length than on flat surface. And these processes are highly exothermic with about -1.46 eV for the fourfold step and -1.91 eV for the threefold step. We are not able to determine which pathway is the most favorable routine based on the final states, since the adsorption energies of final states are very close. The energy barrier of flat routine is about 1.17 eV, which is much higher than the energy barriers on step sites. Thus, the step sites routines are more favorable. As the the difference between fourfold and threefold step routines, the NO prefer to adsorb on the fourfold step rather than threefold step. The adsorption energy on threefold step is even 0.15 eV higher than on flat hcp site. That makes the threefold step routine is less favorable than fourfold step routine.

4.6. Ru (10 $\bar{1}9$) Terrace effect

It's obvious that the Ru (10 $\bar{1}5$) doesn't include a considerable terrace width, while Ru (10 $\bar{1}9$) surface has a four-atom-wide terrace that is more reliable to study the terrace effect. To get a better description of the terrace, Ru (10 $\bar{1}9$) was used to study the NO reactivity on the terrace.

For the relatively equivalent adsorption sites between Ru(10 $\bar{1}5$) Surface and Ru (10 $\bar{1}9$) Surface, as shown in below, the energy difference are not significant. As the results suggested, all the species near the (10 $\bar{1}9$) step (N atom, O atom and NO molecule) have almost identical adsorption energy to Ru (10 $\bar{1}5$) surface's results. In general, the Ru (10 $\bar{1}9$) possesses same property as the Ru(10 $\bar{1}5$) near the step sites.

Table 4.5 The calculated geometries, adsorption energies of atomic oxygen & nitrogen, and NO molecule on the Ru (10 $\bar{1}9$) terrace

	Step-HCP	HCP2	HCP3	HCP4
N				
E_{ad}	-0.64	-0.94	-1.02	-0.55
O				
E_{ad}	-2.48	-2.84	-2.94	-2.52
NO				
E_{ad}	-3.01	-2.66	-2.73	-2.43

As for the terrace, it possesses a very close property as the flat Ru (0001) surface. On the Surface (10 $\bar{1}9$), the HCP2 and HCP3 are basically equivalent to Ru(0001) HCP site as the energy difference is only 0.01 eV~0.05 eV. We also calculated the NO dissociation over the terrace. As expected, the NO dissociation energy barrier is also very close to the flat surface's results, which is about 1.15 eV. Thus, the NO reactivity on the Ru terrace follow the behavior on flat surface.

4.7. Reconstruction Ru ($10\bar{1}9$) surface

Previous studies show that Ru crystals tend to form double atom steps. For the Ru ($10\bar{1}9$) crystal, analysis of the LEED behavior suggests the step-doubling reconstruction [61].

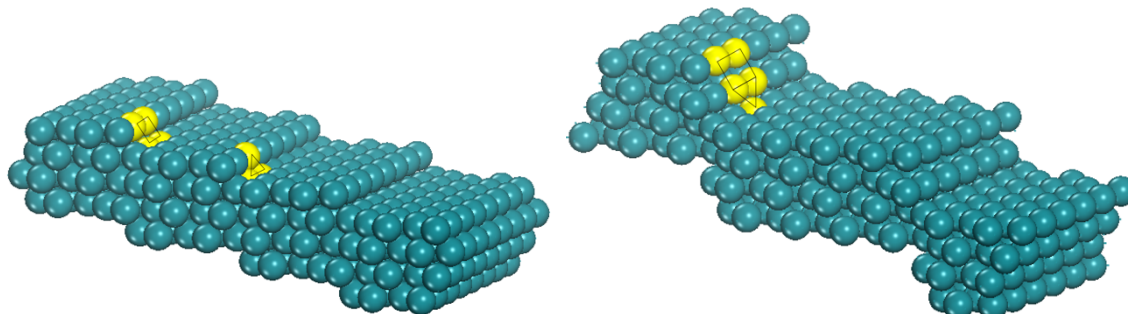


Figure 4.4 Ru ($10\bar{1}9$) Ideal surface (a) and experimentally found reconstruction (b) Ru ($10\bar{1}9$) surface

The Ru crystal was cut along the ($10\bar{1}9$) direction. When the crystal was cleaved, its crystal surface would expose five-atom wide (0001) terraces, separated by on-atom high steps of the ($10\bar{1}0$) orientation. The steps are equivalent to the step ($10\bar{1}5$) surface, that one step has threefold Ru atoms, and other has fourfold Ru atoms, as shown in the Figure 4.4 (a)

It's found experimentally that step-doubling reconstruction took place by an analysis of LEED behavior. When the double-atom step is formed, the reactants were tested that the double-atom step also shows a high reactivity for NO dissociation. Since the steps are composed of Ru ($10\bar{1}0$), we will illuminate the origin of the step effect and propose a new finding that the ($10\bar{1}0$) surface is the active surface for NO dissociation.

5. NO dissociation on Surface ($10\bar{1}0$)

In this part, we will compare the pathways for NO dissociation with several adsorption configurations based on a DFT description of the reaction paths. Two main typical adsorption states as initial state will be considered, one is the molecule vertically adsorbed on the surface, the other one is parallel adsorb on the surface.

5.1. Model

For all the calculations, a p (3×3) unit cell has been used, the slabs, clean Ru surface, was modeled using four atomic layers. The two bottom layers were fixed, the two top layers and adsorbates were totally relaxed. The K-point mesh of $3\times 3\times 1$ was used. The geometry optimization used same method (CG and Quasi-Newton) as previous work. For the transition state search, the NEB method was used to find the saddle point of reaction path connected by a band of images between initial state and final state.

The Ru ($10\bar{1}0$) surface is more open than the close-packed surface, as shown in Figure 5.1. As we expected, the calculated cohesive energy of most common exposed surface Ru (0001) is 6.242eV, that is slightly higher than ($10\bar{1}0$) surface which is 6.045eV. In addition, LEED analysis [62] confirmed that there exist stable clean Ru ($10\bar{1}0$) surface without any further reconstruction. In the Ru ($10\bar{1}0$) surface, there are three types of equivalent sites, fourfold hollow site, hcp site and fcc site, which are the possible binding sites for NO, as shown in Figure 5.1(c). The fourfold site is composed of four Ru atoms, two of them are 9-coordinated and rest of them are 8-coordinated. The hcp site is consisted of two 9-coordinated Ru atoms and one 8-coordinated atom, which fcc site is two 8-coordinated and one 9-coordinated.

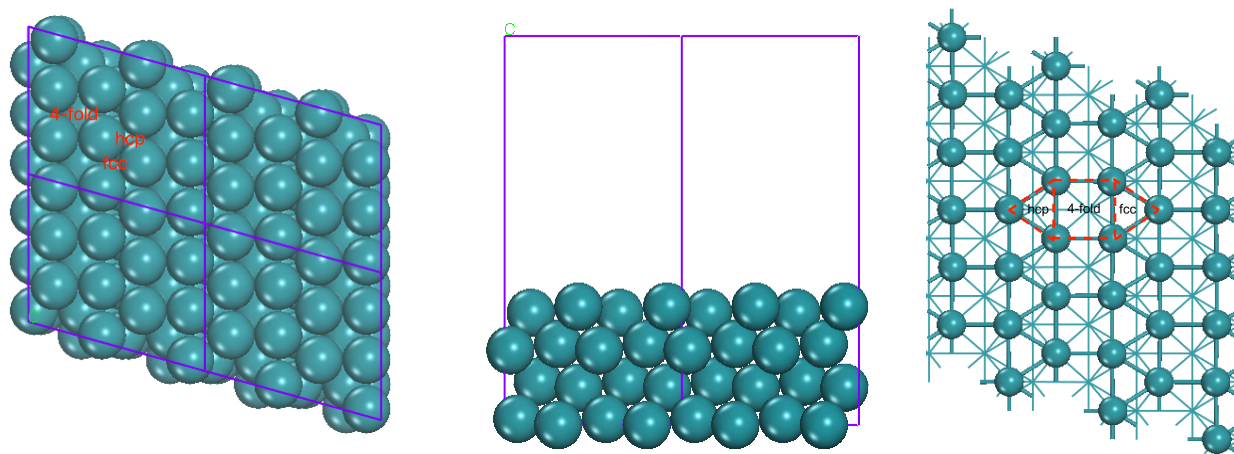


Figure 5.1 Ru ($10\bar{1}0$) surface top view (a) , side view (b), first layer of surface (c)

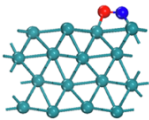
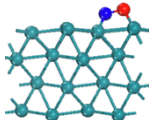
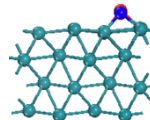
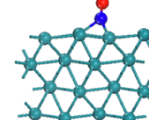
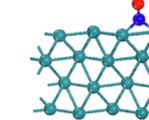
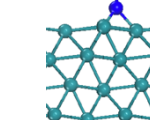
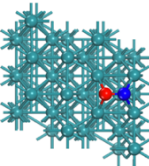
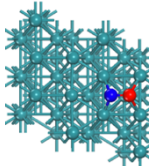
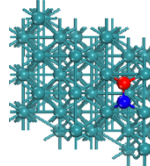
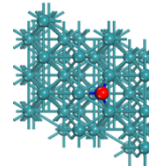
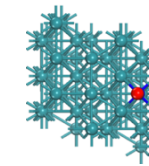
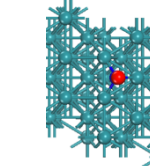
5.2. Molecular Adsorption of NO on Ru surface

The molecular adsorption of NO on different sites on Ru ($10\bar{1}0$) surface is fairly significant to study the dissociation since the initial states of NO molecule affect the following redaction paths of the reduction process.

For low-coverage adsorption (1/9 ML) on the Ru ($10\bar{1}0$) surface, all the possible adsorption sites for the NO molecule are investigated, which are shown in following Table 5.1. Compared to the most stable adsorption site on Ru (0001) surface (hcp site, $E_{ad} = 2.68$ eV), all the adsorption configurations on Ru ($10\bar{1}0$) surface are more stable. There is no significant energy difference among various adsorption structures. However, the NO molecule adjacent on the two Ru bridge sites have the geometrical advantage to dissociate to atomic oxygen and nitrogen, while the vertically adsorbed molecules show less possibilities to dissociate, that will be discussed in following paragraph.

For the NO molecule parallel adsorb on the fourfold site, there are three possibilities for the NO binding with the fourfold site as shown in Table 5.1. Not surprisingly, the adsorption energies of these three configuration are quite close which are from -2.72 to -2.78 eV. We found no stable adsorption configurations for NO parallel adsorption on hcp and fcc site, which is same as the results on flat Ru (0001) surface. For the NO molecule vertically adsorbs on the Ru ($10\bar{1}0$) surface, it can adsorb on fourfold site, hcp and fcc sites. Interestingly, the adsorption energy (-2.82 eV) on the threefold sites (fcc and hcp) are very close, that is different from the adsorption preference on flat Ru (0001) surface. The NO molecule can also adsorb on the fourfold site vertically, that its adsorption energy is quite close to parallel adsorption, but 0.14 eV slightly higher than threefold site. The bond lengths of N-O are listed in Table 5.1. As results shown, for the parallel adsorption on the fourfold, the optimal N-O distances are about 1.375 to 1.393 Å, which are a bit longer than the bond lengths for the vertical adsorption. (1.227 Å for hcp, 1.231 Å for fcc and 1.250 Å for fourfold)

Table 5.1 The calculated NO adsorption geometries, adsorption energies (eV) and bond length (Å)

	Fourfold-1	Fourfold-2	Fourfold-3	Hcp-vtc	Fourfold-vtc	Fcc-vtc
Side view						
Top view						
E_{ad} (eV)	-2.78	-2.72	-2.78	-2.82	-2.68	-2.83
N-O bond (Å)	1.375	1.393	1.378	1.227	1.250	1.231

Bader charge analysis show that when the NO adsorb on the 4-fold site, the N atom attract 0.74 e (0.76e for fourfold-2), O atom attract 0.16 e (0.16 e for fourfold-2) from the coordinated Ru atoms, which lose about 0.20-0.23 e. Regarding the vertical adsorption, the electron transfer behaves similar to the Ru (0001) surface, which the N atom attract 0.6 e from the adjacent Ru atoms. The N on fcc site of Ru (0001) surface gain about 0.52 e.

5.3. NO adsorption transformation

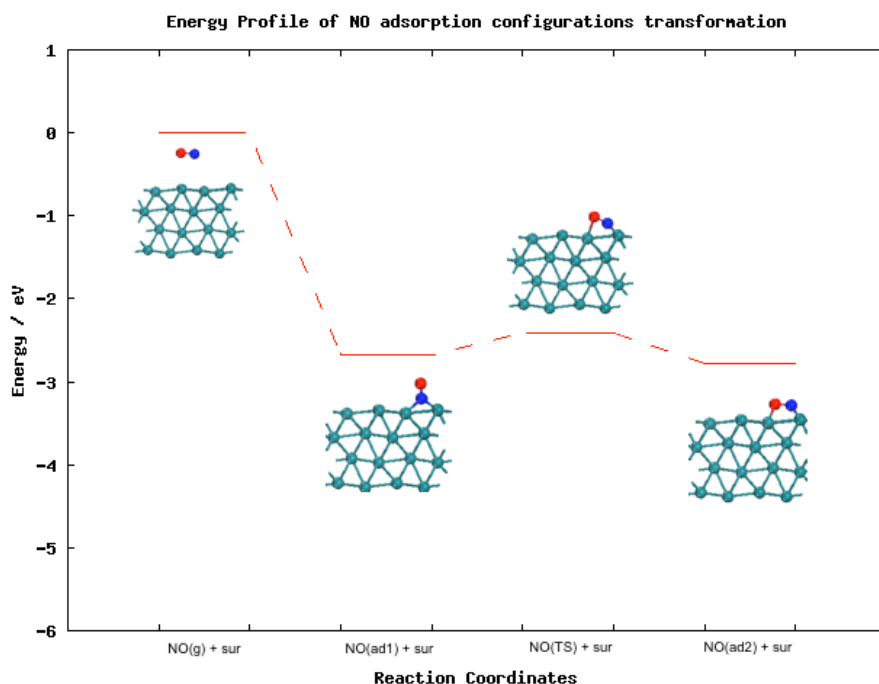


Figure 5.2 Energy profile of NO adsorption configuration transformation

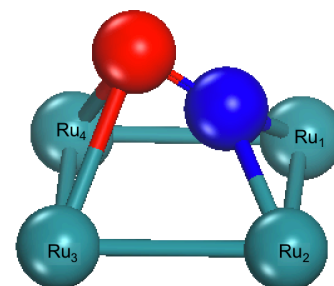


Figure 5.3 Top view of fourfold Ru site with adsorbed NO molecule (Transition state)

Table 5.2 Energy Barrier and Dissociation energy of NO decomposition on Ru(101) surface

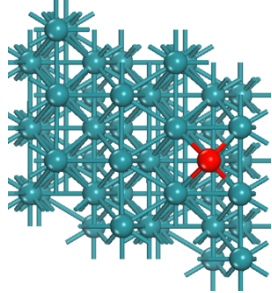
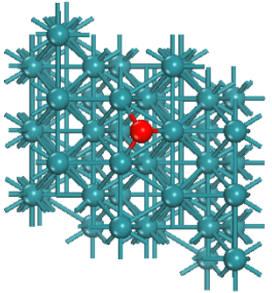
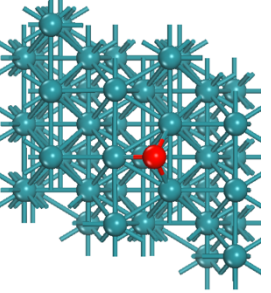
	E_{ad} (eV)	N-O (Å)	Ru(3,4)-O (Å)	Ru(1,2)-N (Å)
NO(vtc) + sur	-2.68	1.250	-	2.144 2.146 2.264 2.262
NO(ts) + sur	-2.42	1.307	2.508, 2.379	1.971, 1.963
NO(para) + sur	-2.78	1.375	2.175, 2.169	1.978, 1.978

Due to the fact that NO molecule can adsorb both parallel and vertical on the surface, there could be a possibility for the molecule to transfer to more energetically stable state. The energy profile of NO adsorption transfer from vertical adsorption state to parallel state is shown in the Figure 5.2. For the NO fourfold-vtc adsorption state, it is 0.1 eV less energetically favorable than NO fourfold-1 adsorption state. To transform the adsorption state from the vertical adsorption to parallel adsorption, it has to overcome an energy barrier of 0.26 eV. The N-O bond length is prolonged during this transformation process. The bond length of the initial state is about 1.250 Å. For the transition state, the bond length increases to 1.307 Å. The Ru₃ - O and Ru₄ - O bonds are about 2.508 Å and 2.379 Å, which nearly form a Ru-O bond. Meanwhile, the Ru-N bonds are shortening from 2.146 Å (Ru₁ - N) and 2.144 Å (Ru₂ - N) to 1.971 Å (Ru₁ - N) and 1.963 Å (Ru₂ - N). After the reaction reaches the parallel adsorption state (fourfold-1), the Ru₃ - O and Ru₄ - O bonds are formed with bond lengths of 2.175 Å and 2.169 Å. The bond lengths of Ru-N, which are both 1.978 Å, are quite close to the transition state.

5.4. Atomic adsorption

To determine the adsorption preference of the dissociated product, we investigated the atomic chemisorption of the oxygen and nitrogen. The adsorption energy for the binding structures are listed in following Table 5.3.

Table 5.3 The calculated geometries, adsorption energies of atomic oxygen and nitrogen on the Ru (10 $\bar{1}$ 1) terrace

Geometry			
	fourfold	fcc	hcp
$E_{ad}(O)$ (eV)	-2.73	-2.98	-2.75
Ru-O bond (Å)	2.224 2.256 2.085 2.091	2.034 2.033 2.037	2.000 2.050 2.052
$E_{ad}(N)$ (eV)	-1.01	-0.78	-0.71
Ru-N bond (Å)	2.114 2.105 2.033 2.033	1.930 1.944 1.949	1.943 1.943 1.976

As shown in the Table 5.3, for the N atomic adsorption, the most favorable adsorption site is fourfold site, while for the O atom, it is more stable to bind with Ru atoms on fcc site.

For oxygen atomic adsorption, the adsorption preference order is: $fcc > hcp \approx fourfold$. For the most stable adsorption site fcc, the binding energy is about -2.98 eV, and the bond lengths of Ru-O are 2.034, 2.033 and 2.037 Å, respectively, which are slightly shorter than the bond length in flat Ru (0001) surface (2.05 Å). Not like the adsorption preference order in flat Ru (0001) surface, the oxygen binding with hcp site is less favorable than on fcc site. The oxygen atomic adsorption energy on hcp site is about -2.75 eV, which is lower than fcc site oxygen adsorption energy (-2.90 eV) on Ru (0001) surface. Similarly, the bond length of Ru-O in (10 $\bar{1}$ 0) surface is also slightly shorter than in Ru (0001) surface. Regarding to the fourfold adsorption, the oxygen atom almost stays in the mid of the fourfold Ru atoms. In fact, the bond lengths of Ru-O close to the fcc site are shorter than the Ru-O bond close to the hcp site by about 0.07 Å. The reason for this imbalance may attribute to the Ru atoms close to fcc site are 8-coordinated, meaning that these two Ru atoms may be more active, leading to a relatively shorter bond length.

As for the N atomic adsorption, the order, different from the O atomic, is: $fourfold > fcc \approx hcp$. In general, the bond lengths are quite similar to the trend of O atomic adsorption. Same explanation can be applied to the N atomic adsorption. However, the most stable configuration for the N atom adoption is on the fourfold site, and its adsorption energy is about -1.01 eV, which is close to the most stable adsorption energy (-1.06 eV on hcp site) on Ru (0001) surface.

The reason why the adsorption energies on fcc site is lower than hcp is because of the surface Ru coordination number. Since hcp site is consisted of two 9-coordinated Ru atoms and one 8-coordinated atom, which fcc site is two 8-coordinated and one 9 coordinated. The low-coordinated Ru is reported to be more active on the step edge [3]. In the open flat Ru (10 $\bar{1}$ 0) surface. The low-coordinated Ru atoms also possess same property.

5.5. Atomic Diffusion

In the Figure 5.4, the diffusion potential energy curves have been reported, based on the chemisorption energies of N and O shown in the Table 5.3 above. The six diffusion routines have been considered, diffusion between hcp and fcc site, fcc and fourfold site, fourfold and hcp site. The atomic diffusion energy barriers are listed in the Table 5.4.

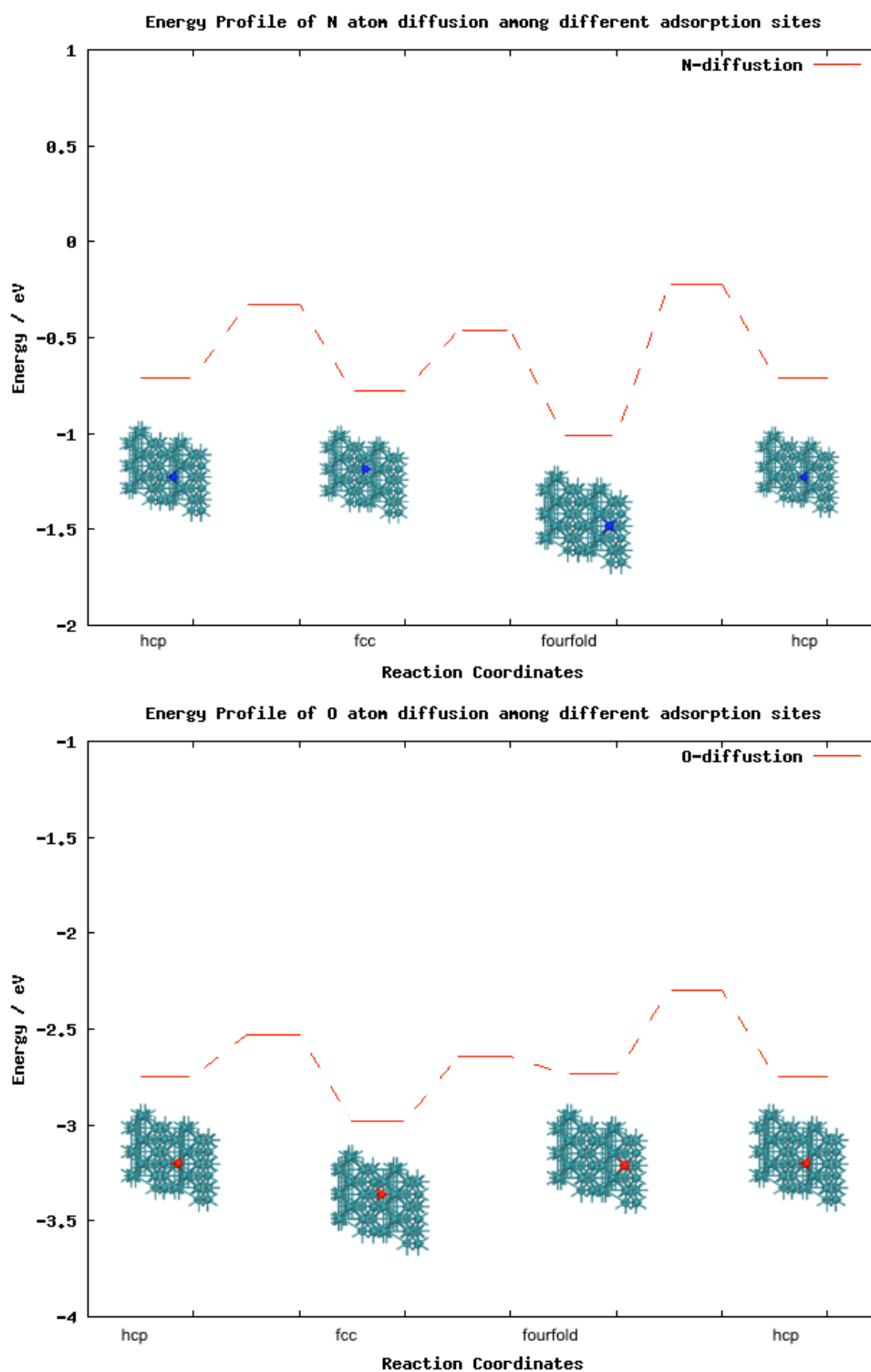


Figure 5.4 Atomic N (up) O (down) diffusion between different adsorption sites

Table 5.4 Atomic N (O) diffusion barrier (eV) on Ru(10 $\bar{1}$ 1) surface

	N	O
Hcp-fcc	0.38	0.22
Fcc-hcp	0.45	0.45
Fcc-fourfold	0.32	0.34
Fourfold-fcc	0.55	0.09
Fourfold-hcp	0.79	0.43
Hcp-fourfold	0.49	0.45

The energy barriers for the N diffusion are ranged from 0.32 to 0.79 eV. When the N atom diffuses from the most stable fourfold site to hcp site, it is hindered an energy barrier of 0.79 eV. For the rest of the diffusion routines, the energies are about 0.32-0.55 eV, which is not difficult to make the N atom diffuse among these sites. The relatively higher energy barriers of the fourfold-hcp and fourfold-fcc routines indicate that the N atoms, once adsorbed on the fourfold site, may hardly diffuse to other sites.

For the O atom, the diffusion energy barriers are about 0.09 to 0.45 eV. The relatively lower energy barriers may make the O easily transfer to the adsorption site nearby. Since the energy differences among all the adsorption site are not considerable, all the sites could store the oxygen atomic species. Compared to the flat Ru (0001) surface, the surface oxygen (or nitrogen) will diffuse from the fcc site to the hcp site, leading all the hcp will be covered first. Since the hcp site is the most active site on the flat surface, when the surface oxygens bind with hcp sites, the active centers will be blocked.

5.6. NO Dissociation

For the dissociation pathways on the Ru (10 $\bar{1}$ 0), four different reaction paths involving different initial adsorption states are studied. Three more favorable pathways indicate the NO tend to dissociate on fourfold site, one pathway implies that vertical adsorption state is not favorable for the NO dissociation.

Firstly, the dissociations of NO on the 4-fold site are studied. As the NO adsorption results suggested, for the initial state, the NO can adsorb on the fourfold site parallel and vertically. For the final state, we consider the co-adsorption of N on fourfold site and O on hcp site. The energy profile for both routines are shown in the figure 5.5, and their corresponding energies, and bond length information are listed in the Table 5.5.

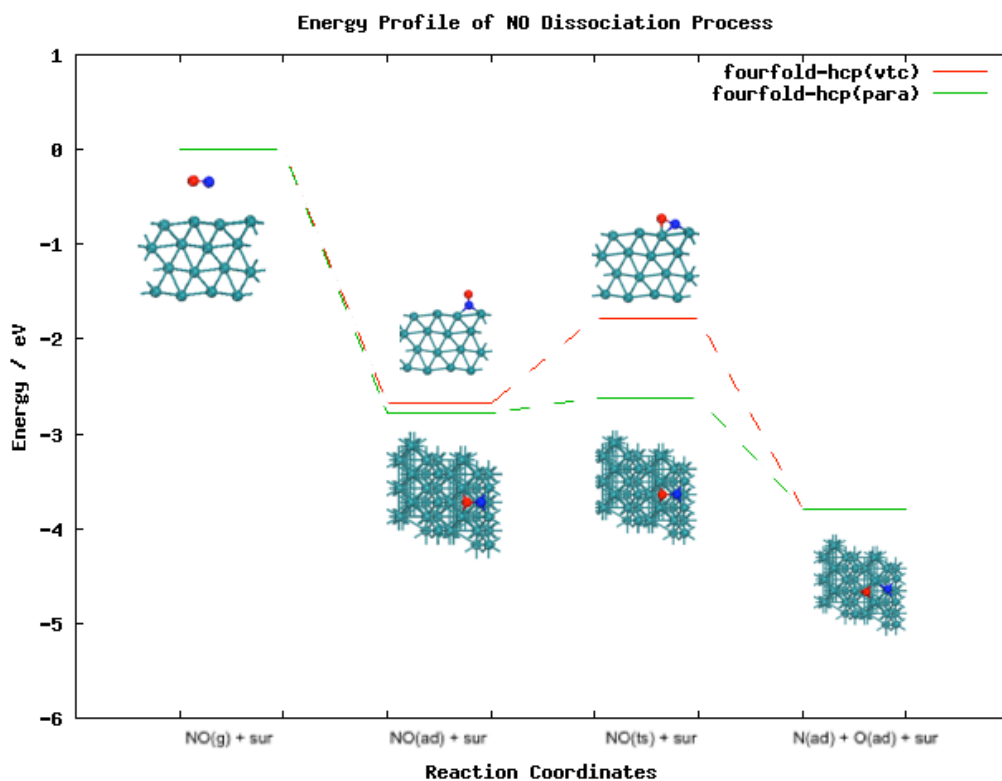


Figure 5.5 The compilation of NO dissociation between vertical adsorption routine and parallel routine

Table 5.5 Energy Barrier and Dissociation energy of NO decomposition on Ru(10 $\bar{1}$ 0) surface

	4-fold		4-fold-vtc	
	E_{ad}	N-O Distance(Å)	E_{ad}	N-O Distance (Å)
NO(ad) + sur	-2.78 eV	1.376	-2.68 eV	1.250
NO(ts) + sur	-2.62 eV	1.555	-1.78 eV	1.497
N(ad) + O(ad) + sur	-3.80 eV	2.621	-1.78 eV	2.621
Transition Barrier	0.16 eV		0.90 eV	
Dissociation Energy	-1.02 eV		-1.12 eV	

The parallel adsorption is more energetically favorable than vertical adsorption by 0.10 eV. The N-O bond length of parallel adsorption is 1.376 Å, which is longer than vertical adsorption state (1.250 Å). For the parallel dissociation routine, the O in the molecule dissociates to the hcp site with the assistance of bridge Ru atoms. For its transition state, the distance of N-O is prolonged to 1.555 Å. To activate the NO molecule, it is hindered a tiny energy barrier of 0.16 eV. The dissociated atoms are separated on fourfold site and hcp site. Since the co-adsorption of O on hcp site and N on fourfold site is favorable. We considered this as final state. The whole process from adsorbed NO to separated N atom and O atom is exothermic (-1.02 eV).

For the vertical adsorption routine, the NO bond length is 1.250 Å, which is close to other vertical adsorption states. The NO can strongly bind with fourfold site with an adsorption energy of -2.68 eV. For the transition state, the vertical NO molecule is bended to hcp site. The N-O bond increases to 1.497 Å. Compared to the parallel adsorption routine, the vertical adsorption routine has to overcome about 0.90 eV to separate N and O atom. Since the vertical adsorption energy is less stable than parallel adsorption by 0.10 eV, the dissociation process is more exothermic (-1.12 eV).

As adsorption results shown, the NO has three types of parallel adsorption states, we have illustrated one reaction routine (fourfold-1). The rest of two reaction pathway are given in the following Figure 5.6 and corresponding energies in Table 5.6.

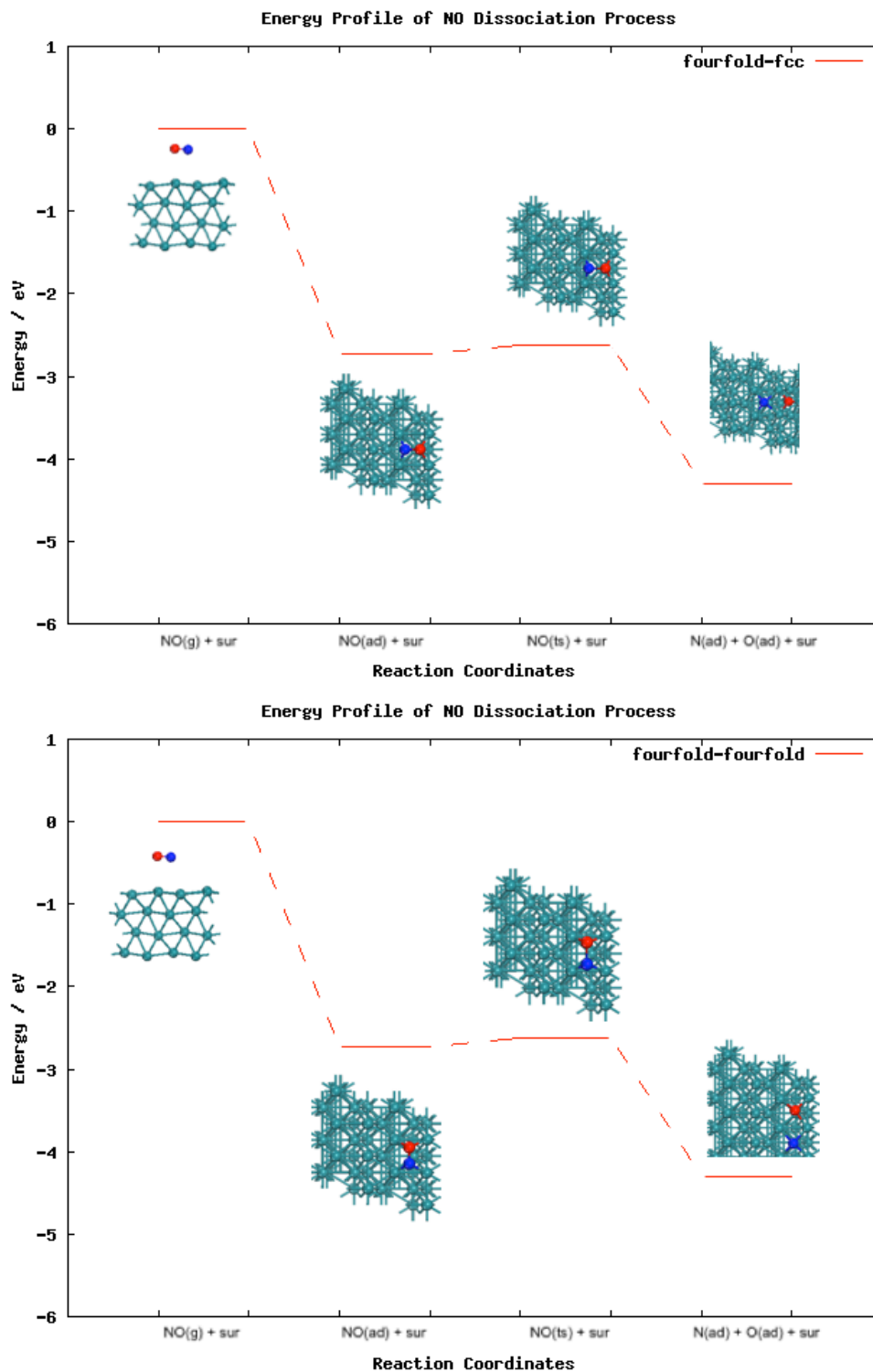


Figure 5.6 The reaction energy profile of NO dissociation for 4-fold-2 pathway (up) and 4-fold-3 pathway (down)

Table 5.6 Energy barrier and dissociation energy of NO decomposition on Ru(10 $\bar{1}$ 0) surface

	4-fold-2		4-fold-3	
	E_{ad}	N-O Distance(Å)	E_{ad}	N-O Distance (Å)
NO(ad) + sur	-2.72	1.393	-2.78	1.378
NO(ts) + sur	-2.63	1.580	-2.58	1.779
N(ad) + O(ad) + sur	-4.30	2.728	-4.33	3.100
Transition Barrier		0.09		0.20
Dissociation Energy		-1.58		-1.55

For the fourfold-2 routine, the NO molecule, compared to fourfold-1 state, reversely adsorbs on the fourfold site, that the O atom is close to fcc site. The adsorption energy of initial state is -2.72 eV. The final state for this path is that the N adsorb on fourfold site and O bind with hcp site. Not surprisingly, the separated N(fourfold) + O(fcc) state possess even more stable adsorption energy (-4.30 eV) than N(fourfold)+O(hcp) site by 0.50 eV. During the dissociation process, the adsorbed NO molecule are activated by the bridge Ru atoms (part of fourfold site), the bond length increases from 1.393 Å to 1.580 Å. As we discussed before, the 8-coordinated Ru atoms are more active. For the process involving the 8-coordinated Ru atoms as bridge atoms, its reaction barrier, only 0.09 eV, is even lower than fourfold-1 pathway.

For the fourfold-3 pathway, the direction of NO adsorption is along the fourfold direction, the O and N are both bind with one 9-coordinated and one 8-coordinated Ru atom. The final state is considered as both atomic species are on fourfold site. Since the distance of N-O in final state is as long as 3.100 Å, which is larger than N-O distance in other co-adsorption states, meaning the relatively lower interaction between two atoms, the adsorption energy (-4.33 eV) of final state (N(fourfold) + O(fourfold)) is even lower than previous one. The dissociation energy barrier, as we expected, is also quite small. It is hindered an energy barrier of 0.20 eV to dissociate NO molecule to N and O atom on both fourfold site.

6. Theoretical study of cubane-type $[\text{Ni}_4\text{Cl}_8]$ complexes' magnetic properties

6.1. Research Motivation

A new Ni_4Cl_8 cubane-type complex with the formula $[\text{Ni}(\mu_3 - \text{Cl})\text{Cl}(\text{HL} \cdot \text{S})]_4$, where $\text{HL} \cdot \text{S}$ represents a pyridyl-alcohol-type ligand with a thioether function group, is characterized by a ferromagnetic coupling and is considered to be a single-molecule magnet (SMM) [64]. The complex is composed of Ni_4Cl_8 cluster and 4 $\text{HL} \cdot \text{S}$ ligands as Figure 3 shown. There is a sulfur atom that exhibits a high affinity for gold, thus allowing the covalent binding to the surface or acting as a tunneling interface in a single-molecule junction between Au electrodes.

Experimentally [64], XPS results show that the sulfur atom in the ligand will bind with the gold surface. It has been found in adsorption experiments that the bare $\text{HL} \cdot \text{S}$ ligand without central cube can bind on the Au (111) surface. The XPS results showed that the doublet at 163.1 eV, which is responsible for 52.9% of the total population, is recognized as binding for a thioether group. And doublets at 162.1 and 161.1 eV are responsible for the remaining 47.1% of the signal, which are attributed to a thiol group bound to gold surface. For the intact $\{\text{Ni}_4\}$ it is geometrically impossible for all four ligands to bind to the gold surface. In fact, from the DFT calculation, we found that only one ligand will attach to the surface. XPS spectra estimates that a weight of 50-75% unbound species, which indicates that the $\{\text{Ni}_4\}$ loses at least some of its ligands when adsorbing on the surface.

Based on this background, we want to study the possibility of observing SMM behaviors when the $\{\text{Ni}_4\}$ loses some of its ligand from 1 to 4; which is the stable adsorption of the complex on Au (111) surface; and if adsorption affects the magnetic properties.

This report is arranged in the following aspects: 1. The molecular study regarding the first research question, 2. The surface study concerning the second question, 3. The challenges and the difficulties for the last question.

6.2. Theoretical background

All calculations for the complexes were carried out with the ORCA code [65]. For the geometries optimization, we used B3LYP functional [66]. Since the vdW interaction is significant in this system, the D3 method of Grimme [67] was used for the dispersion correction. The complex was prepared in the solvent. Thus, we also included the solvation effect of CH_2Cl_2 using SMD solvation model [68] For the basis set, def2-tzvp, and corresponding RI-J auxiliary [69] were used.

The CASSCF calculations on the optimized geometries were performed to get better description of the energy differences. For active space of each metal center, we considered two electrons in a two orbitals, meaning that for the $\{\text{Ni}_4\}$, the CAS (8,8) were used, for the $\{\text{Ni}_2\text{Zn}_2\}$ model, CAS(4,4) were used. The spin-orbit coupling matrix was constructed within the active space and diagonalized to calculate the zero field splitting (ZFS) parameters.

6.2.1. Heisenberg Hamiltonian

The magnetic exchange interaction between two magnetic center is described by the following Spin-Hamiltonian

$$H = -J S_a \cdot S_b$$

The Two-J model is used to characterize the magnetic coupling parameters can be expressed as:

$$H = -J_1 \sum S_a \cdot S_b - J_2 \sum S_c \cdot S_d$$

where J is the isotropic exchange coupling constant and S_a, S_b, S_c, S_d are the spins on Ni metal center respectively.

The eigenenergies of the Spin-Hamiltonian are expressed as follows:

$$E(S) = -\frac{J}{2} [S(S + 1) - 2s(s + 1)]$$

Where S represents the total spin of the system and s is the atomic spin. Assuming that the magnetic coupling in the complex is solely a spin exchange interaction between 3d electrons, we obtain the energy difference regarding different spin state, that is known as Lande interval rule,

$$\Delta_{s,s-1} = E(S) - E(S - 1) = -JS$$

6.2.2. Electronic configurations

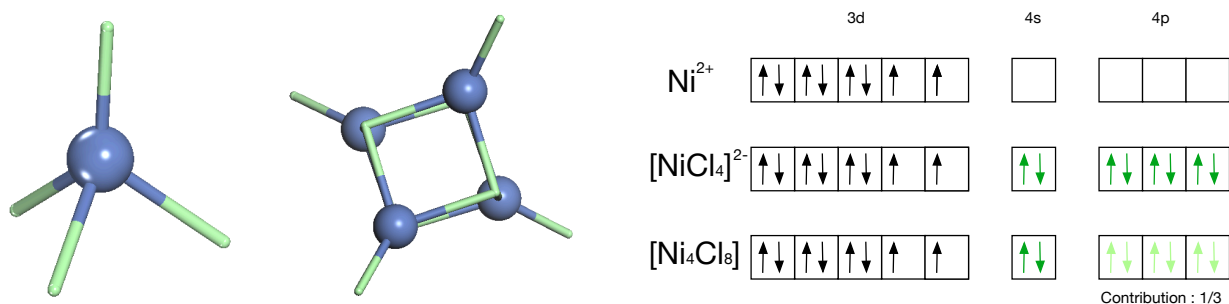


Figure 6.1 Geometries and Electronic configurations of $[\text{NiCl}_4]^{2-}$ and Ni_4Cl_8 , the ball model is Ni and stick is Cl

Starting from the Ni^{2+} cation, the electronic configuration is $3d^8$ for Ni cation. For the $[\text{NiCl}_4]^{2-}$ complex, the Cl anions coordinate with the Ni cation center and form this electronic configuration. The complex is tetrahedral and paramagnetic. The Nickel center is SP^3 hybridization. The geometries and their electronic configurations are given in Figure 1.

Similarly, for the Ni_4Cl_8 cluster, since the bridge Cl is shared by three Ni atoms, thus the contribution to the 4p orbital is only 1/3, the paired electrons from Cl atom are equally distributed in the three Ni atoms. The Ni is distorted SP^3 hybridization. The unoccupied orbitals are able to accept more electrons from the ligands forming $[\text{Ni}(\mu_3 - \text{Cl})\text{Cl}(\text{HL} \cdot \text{S})]_4$ complex.

As shown in the Figure 6.1, there are two unpaired electrons from the Ni center. To extract the J parameter, there are three different spin configurations for the Ni_4 cluster, which are listed in Figure 6.2. The high-spin $S_{\text{HS}} = \uparrow\uparrow\uparrow\uparrow$, the intermediate-spin $S_{\text{IS}} = \uparrow\uparrow\uparrow\downarrow$ and the low-spin state $S_{\text{LS}} = \uparrow\uparrow\downarrow\downarrow$ configurations.

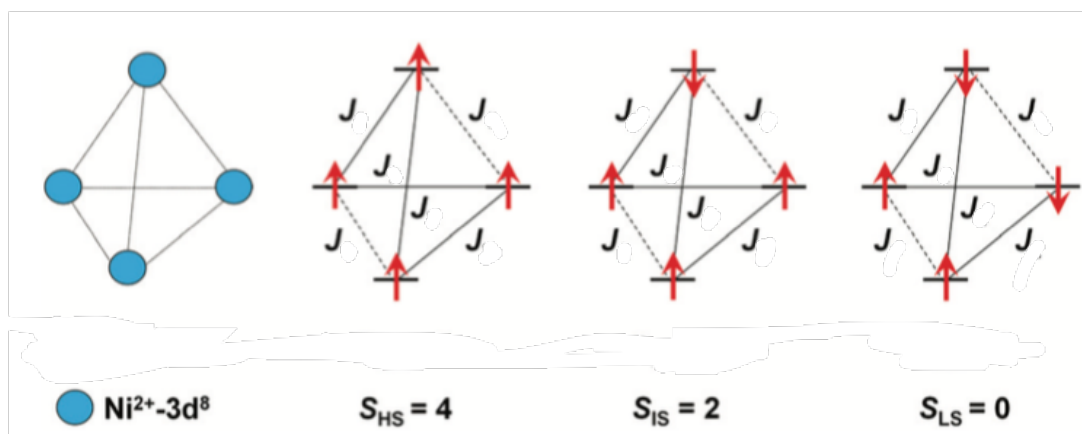


Figure 6.2. Three possible spin-state for the cubane-type $[\text{Ni}(\mu_3 - \text{Cl})\text{Cl}(\text{HL} \cdot \text{S})]_4$. The coupling constants J represents the interactions between the Ni atoms.

For the highly symmetric complex like intact $[\text{Ni}(\mu_3 - \text{Cl})\text{Cl}(\text{HL} \cdot \text{S})]_4$ complex and the bare $\{\text{Ni}_4\text{Cl}_8\}$ center, we can use two- J model and one- J model to describe the system.

For the bare Ni_4Cl_8 structure, since it possesses S_4 symmetry, which means the J constant is identical. According to Heisenberg model, the energy spectrum for Ni^{2+} is:

$$E_{\text{HS}} = -6J \quad E_{\text{IS}} = 0 \quad E_{\text{LS}} = 2J$$

As for the intact $[\text{Ni}(\mu_3 - \text{Cl})\text{Cl}(\text{HL} \cdot \text{S})]_4$ complex, the energy spectrum is:

$$E_{\text{HS}} = -2J_1 - 4J_2 \quad E_{\text{IS}} = 0 \quad E_{\text{LS}} = -2J_1 + 4J_2$$

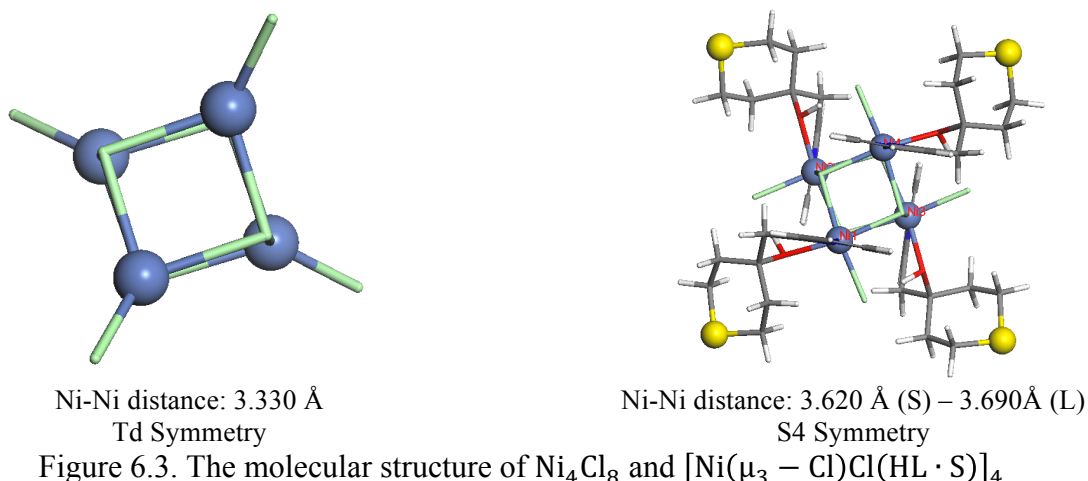
6.2.3. Ni_2Zn_2 and NiZn_3 model

When the $[\text{Ni}(\mu_3 - \text{Cl})\text{Cl}(\text{HL} \cdot \text{S})]_4$ complex loses several ligands, meanwhile it also loses its symmetry. The distance between two Ni atoms are no longer identical. Thus, the Two- J model may fail to describe the magnetic properties accurately. To study these complexes, we use an approximation that replaces two Ni atoms into Zn atoms, that have no unpaired electrons in d orbitals. Using this approach, we can use this Heisenberg model to study their magnetic properties.

To estimate the local D parameter in the Ni atom, the single-ion (local) ZFS was calculated using a NiZn_3 model where the Ni center is in its real molecular environment. The rest of the Ni atoms are replaced by Zn atoms.

6.3. Molecular Results

6.3.1. $[\text{Ni}(\mu_3 - \text{Cl})\text{Cl}(\text{HL} \cdot \text{S})]_x$ ($x = 0, 4$) Result



Firstly, we performed the Ni_4Cl_8 and $[\text{Ni}(\mu_3 - \text{Cl})\text{Cl}(\text{HL} \cdot \text{S})]_4$ and calculations. Then we can compare our $[\text{Ni}(\mu_3 - \text{Cl})\text{Cl}(\text{HL} \cdot \text{S})]_4$ results with previous theoretical and experimental work.

As shown in the Figure 6.3, one has four ligands and one does not coordinate any ligand. The complexes are highly symmetric. The the bare Ni_4Cl_8 is of Td symmetry, and $[\text{Ni}(\mu_3 - \text{Cl})\text{Cl}(\text{HL} \cdot \text{S})]_4$ is of S4 symmetry. The distance between the Ni centers is especially important than other geometry parameter. For the complex with four ligands, the long term Ni-Ni distance is 3.690, and short term is 3.620 which is 10% longer than bare Ni_4Cl_8 core without any ligand. That come from the repulsion between the ligands that prolong the Ni-Cl bond, consequently the distances between Ni atoms increase.

Table 6.1 The energy difference between high spin state and other two spin states, and calculated J parameter for $[\text{Ni}_2\text{Zn}_2\text{Cl}_8](\text{HL} \cdot \text{S})_4$

S Value	DE12(L)/ cm^{-1}	DE14(S)/ cm^{-1}
S=2	0	0
S=1	5.3	4.6
S=0	7.9	6.9
J	2.6	2.3

For the $[\text{Ni}(\mu_3 - \text{Cl})\text{Cl}(\text{HL} \cdot \text{S})]_4$ complex, The energy difference between high spin state and other two spin states, and calculated J parameter for $[\text{Ni}_2\text{Zn}_2\text{Cl}_8](\text{HL} \cdot \text{S})_4$ are listed in the Table 6.1. The computed isotropic coupling constant are both positive. The ferromagnetic solution and a total high-spin ground state $S=4$ have been found in the complex. The energy difference between the lowest $S_{\text{HS}} = 4$ and the intermediate $S_{\text{IS}} = 2$ is 7.4 cm^{-1} from the CASSCF calculations. We used Ni_2Zn_2 to measure the long-term and short-term J value. The Ni(1) and Ni(2) represent the long-term magnetic interaction and Ni(1) and Ni(4) stand for the short-term. For the long-term interaction, the high-spin state is found to be the lowest energy. The energy difference between S=2 and S=1 is 5.3

cm^{-1} , and $S=2$ and $S=0$ is 7.9 cm^{-1} . Thus, the calculated J constants using the the Lande interval rule are $J_1 = 2.6$ $J_2 = 2.3$.

Compared to the experimental value $J=10.6 \text{ cm}^{-1}$, the CASSCF result obvious underestimate the J constants. And the DFT gives $J_{1(\text{PEB0})} = 15.93 \text{ cm}^{-1}$ and $J_{2(\text{PBE0})} = 12.40 \text{ cm}^{-1}$, $J_{1(\text{B3LYP-D3})} = 18.15 \text{ cm}^{-1}$ $J_{2(\text{B3LYP-D3})} = 13.91 \text{ cm}^{-1}$ overestimate the J constants. It's known that CASSCF always underestimate the J constants [71]. Basically, the CASSCF value is 1/5 of experimental value. When we have a J value of 2-3 cm^{-1} , we can believe this complex is ferromagnetism.

For the bare Ni_4Cl_8 , since it is belonged to T_d symmetry group. The optimized geometry gives the Ni-Ni distance of 3.330 \AA . The energy differences between different spin state are calculated under CASSCF and NEVPT2 level as shown in Table 6.2. The most energetic favorable state is low-spin state $S=0$, the energy difference between $S=0$ and $S=2$ is 0.5 cm^{-1} . The high-spin state is 5.5 cm^{-1} higher than the low-spin state. For the NEVPT2 calculation, it gives a relatively higher energy difference, that might give a better description, but unfortunately, we have no experimental result to compare. Since our NEVPT2 calculations for other complexes are not converged, we will study the magnetic properties on the CASSCF level. According to previous studies, NEVPT2 can give a quite close J constant to experimental value. And the NEVPT2 J constant is about 5 times larger than the CASSCF result.

Table 6.2 The energy difference between low spin state and other two spin states, and calculated J parameter for Ni_4Cl_8 under CASSCF and NEVPT2 level.

	DE(CASSCF)/ cm^{-1}	DE(NEVPT2)/ cm^{-1}
S=0(LS)	0	0
S=2(IS)	0.5	5.7
S=4(HS)	2.2	16.7
J	0.3	2

Based on the assumption above, results show that the $S=0$ is the ground state, and calculated J constants is 0.3 cm^{-1} for CASSCF and 2 cm^{-1} for NEVPT2 which lead to paramagnetic.

6.3.2 $[\text{Ni}(\mu_3 - \text{Cl})\text{Cl}(\text{HL} \cdot \text{S})]_x$ ($x = 1, 2, 3$) Result

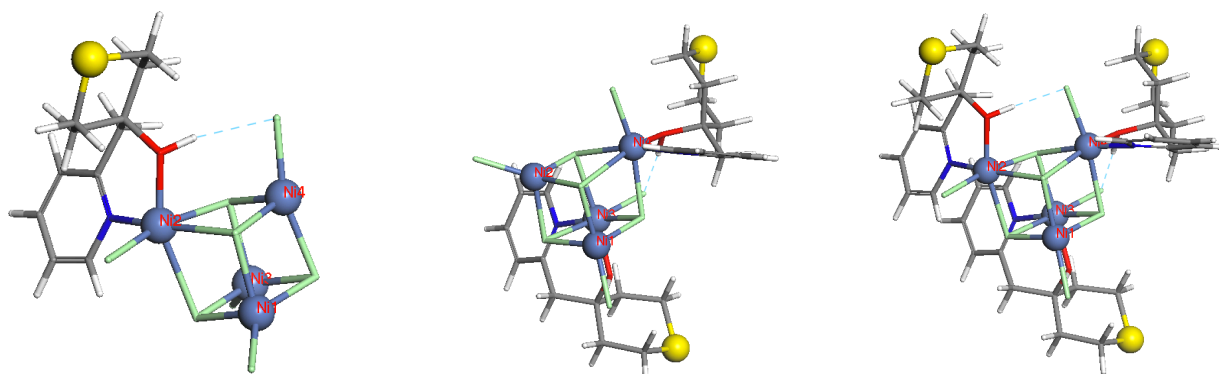


Figure 6.4. Molecular structure of $[\text{Ni}(\mu_3 - \text{Cl})\text{Cl}]_4(\text{HL} \cdot \text{S})_x$ ($x = 1, 2, 3$)

The optimized geometries of $[\text{Ni}(\mu_3 - \text{Cl})\text{Cl}]_4(\text{HL} \cdot \text{S})_x$ ($x = 1,2,3$) are shown in the Figure 4. The four Ni atoms are labeled as Ni1, Ni2, Ni3, Ni4. Since the distance between Ni atoms are essentially important to the magnetic properties. The distance between every two Ni atoms are listed in the Table 6.3. The $D_{x=4}$ represents the difference from the intact complex, $D_{x=0}$ stands for the difference from the bare Ni_4Cl_8 core.

Table 6.3. Comparison between the structural parameter of $[\text{Ni}(\mu_3 - \text{Cl})\text{Cl}]_4(\text{HL} \cdot \text{S})_x$ ($x = 1,2,3$) and intact complex, bare core. Bond distances are given in Å, $D_{x=4}$ stand for the difference between $[\text{Ni}(\mu_3 - \text{Cl})\text{Cl}]_4(\text{HL} \cdot \text{S})_x$ and intact complex, $D_{x=0}$ is compared with bare core.

	X=1			X=2			X=3		
	Dis	$D_{x=4}$	$D_{x=0}$	Dis	$D_{x=4}$	$D_{x=0}$	Dis	$D_{x=4}$	$D_{x=0}$
Ni 1- Ni 2	3.649	0.029	0.319	3.340	-0.280	0.010	3.562	-0.058	0.232
Ni 1- Ni 3	3.326	-0.294	-0.004	3.384	-0.236	0.054	3.377	-0.243	0.047
Ni 1- Ni 4	3.353	-0.337	0.023	3.774	0.084	0.444	3.592	-0.098	0.262
Ni 2- Ni 3	3.718	0.028	0.388	3.655	-0.035	0.325	3.839	0.149	0.509
Ni 2- Ni 4	3.432	-0.188	0.102	3.629	0.009	0.299	3.763	0.143	0.433
Ni 3- Ni 4	3.360	-0.260	0.030	3.780	0.160	0.450	3.685	0.065	0.355

For the first complex, the ligand is attached to Ni2, as bold numbers shown. Compared to the Ni_4Cl_8 bare core, due the interaction of the ligand, the distances between Ni1-Ni2, Ni2-Ni3 and Ni2-Ni4 are prolonged, while because of the H-bond (as blue dash line shown), the increase of Ni2-Ni4 is slightly less significant than others.

For the second complex, the ligands are coordinated with Ni3 and Ni4. Compared to the Ni_4Cl_8 bare core, the distances between Ni1-Ni4, Ni2-Ni3, Ni2-Ni4 and Ni3-Ni4 increase by 0.299 Å to 0.450 Å. The repulsions between the ligands prolong the the distances between Ni atoms.

For the third complex, only the Ni1 atoms is not attached with ligand. Not surprisingly, compared to the distance in bare core, all these distances are longer. Since Ni1 atom doesn't coordinate with ligand, leading the distance between Ni1 and other Ni atoms are shorter than the distance in $[\text{Ni}(\mu_3 - \text{Cl})\text{Cl}]_4(\text{HL} \cdot \text{S})_4$ complex.

Table 6.4. Energy difference of $[\text{Ni}_4\text{Cl}_8](\text{HL} \cdot \text{S})_x$ ($x = 0,1,2,3,4$) between different spin state (cm⁻¹)

	X=0	X=1	X=2	X=3	X=4
S=4	2.2	0	2	0	0
S=2	0.3	6.1	0	2.7	7.4
S=0	0	9.9	4.6	8.9	17.3

As shown in the Table 6.4, for the bare $[\text{Ni}_4\text{Cl}_8]$, the low-spin state is calculated to be the most stable state. As previous mentioned, the $[\text{Ni}_4\text{Cl}_8]$ is paramagnetic. For the rest of the complexes with ligand ($x=1,3,4$). The high-spin states have the lowest energies. Since for the geometries of complexes ($x=1,2,3$) are not symmetric. We haven't used Two-J model to calculate the J constants. To illuminate the spin-spin coupling between different magnetic centers, we performed the energy difference calculations using Ni_2Zn_2 model. The calculated energy difference between lowest energy spin state and other two spin state are listed in the Table 6.5.

Table 6.5 The energy differences between most stable spin state and other two spin states, and calculated J parameter for $[\text{Ni}_2\text{Zn}_2\text{Cl}_8](\text{HL} \cdot \text{S})_x (x = 1,2,3)$

		DE12/cm ⁻¹	DE13/cm ⁻¹	DE14/cm ⁻¹	DE23/cm ⁻¹	DE24/cm ⁻¹	DE34/cm ⁻¹
X=1	S=2	0	0	0	0	4.6	0
	S=1	2.2	3.8	2.6	3	1.5	6.1
	S=0	3.3	5.6	3.9	4.6	0	9.1
	J	1.1	1.9	1.3	1.5	-1.5	3.04
X=2	S=2	0	0	0.8	1	0.8	0
	S=1	0.3	2.9	0	0	0	2.9
	S=0	0.5	4.3	3	3.4	1.1	4.3
	J	0.16	1.45	-0.4	-0.5	-0.4	1.45
X=3	S=2	0	5.5	0	0	0	0
	S=1	4.2	1.8	4.9	2.4	3.8	4.6
	S=0	6.3	0	7.4	3.7	5.6	7
	J	2.1	-1.8	2.45	1.2	1.9	2.3

For the complex (x=1), the measured J constants are ranged from -1.5 to 3.04 cm⁻¹. The numerical average J constant is 1.22 cm⁻¹.

For the complex (x=2), it's found that the intermediate spin state is the most stable state. That is in agreement to the Ni₂Zn₂ model's results. The calculated J constants between Ni1-Ni-4, Ni2-Ni3 and Ni2-Ni4 are negative. In addition, for these three configurations, the intermediate spin states (S=1) are also found to be the most stable states. The numerical average J constant is 0.29 cm⁻¹, leading to a paramagnetic property.

For the complex (x=3), the magnetic behavior is quite similar to the x=1. For most of the configurations, the high-spin state is the most stable one, except for the Ni1-Ni3 configuration. The calculated J constants are slightly higher than X=1's results. The numerical average J constant is 1.35 cm⁻¹.

Obviously, the ligand affect the magnetic property of the [Ni₄Cl₈], to confirm and study how ligand influence the magnetic property of the molecule. We extract the single-ion ZFS parameter from the [Zn₃Ni] model. The ZFS parameters are listed in the Table 6.6.

Table 6.6 The single-ion ZFS parameter from Zn3Ni model(cm-1)

	Ni1	Ni2	Ni3	Ni4
x=1	-0.004	-0.167	-0.004	-0.091
x=2	-0.004	-0.002	-0.305	-0.388
x=3	-0.005	-0.075	-0.075	-0.036
x=4			-0.790	

Interestingly, for the calculated ZFS parameter from [Zn₃Ni] model, when the Ni atoms are coordinated with the ligands, the ZFS parameters are more significant than those without ligands. For those Ni atoms not binding with ligands, the calculated ZFS parameter are found nearly zero. Based on all these results we have, we believe that the ligands are the origin for the [Ni₄Cl₈] core to possess magnetic property. Generally speaking, the more ligands have, the higher magnetic interaction between the magnetic centers.

6.4. $[\text{Ni}(\mu_3 - \text{Cl})\text{Cl}(\text{HL} \cdot \text{S})]_x$ ($x = 1, 2, 3$) adsorption on Au (111) surface

6.4.1. Au bulk and surface optimization

The Gold bulk is face centered cubic (fcc) as shown in Figure 6.5(a). Fitting by the Murnaghan Equation of State to the calculated total energies at different lattice parameters, the calculated lattice constant is 4.180 Å which is slightly larger than experimental value of 4.080 Å.

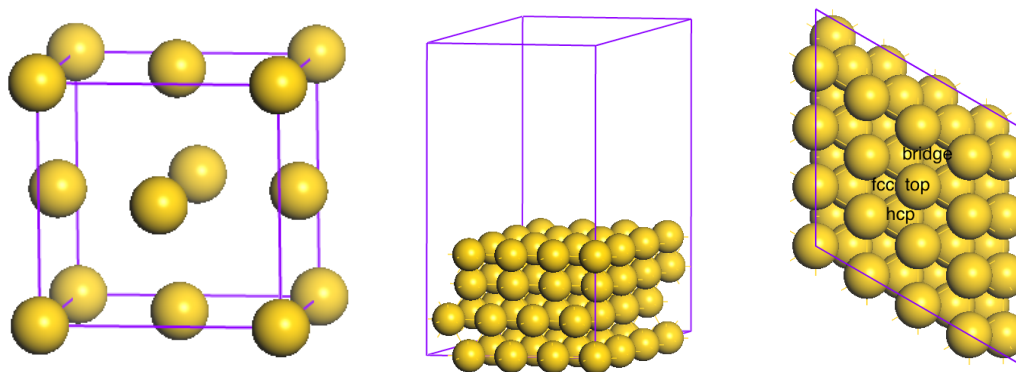


Figure 6.5 Unit cell of Gold Bulk(a), Au (111) side view (b), Au(111) top view (c)

The slabs are separated by about 30 Å of vacuum since the adsorbates is really large. For the surface and adsorption calculation using a p(4x4) slab for ligands, p(5x5) slab for the complex $[\text{Ni}_2\text{Zn}_2\text{Cl}_8](\text{HL} \cdot \text{S})_x$ ($x = 1, 2, 3$). The K-points used 6x6x1 to optimized the surface, while only gamma point was used for the optimization due to the limitation of computational time. There are four gold atoms layers, for the p(4x4), each layer has 16 atoms (Figure 5 b,c); p (5x5) has 25 atoms. The bottom two layers are fixed and the top two layers and adsorbates are fully relaxed.

6.4.2. Ligand adsorption

Before we study the adsorption of the intact complex, we first try to adsorb the ligands on the Au (111) surface. The adsorption sites were tested on hcp, fcc, bridge and top site, as shown in Figure 6.5 (c). According to the XPS results, it detects three different signal of the ligand adsorption. The first one is thioether functional group binding with gold surface, rest of two are thiol functional group.

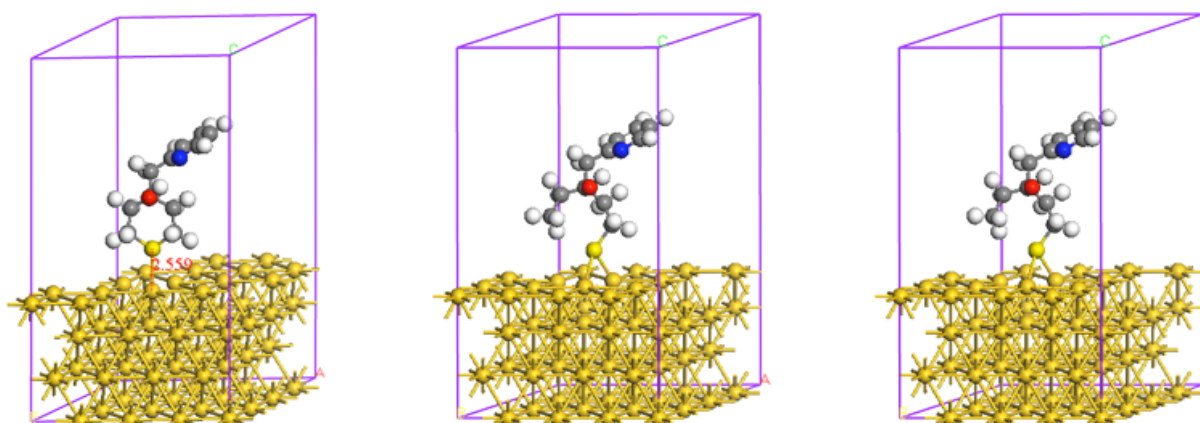


Figure 6.6 The structure of ligand adsorption on Au (111) surface, the first on is thioether formation,

the last two are thiol formation.

After optimization, for the thioether functional group adsorption, the sulfur atom prefers to adsorb on the top site, the bond length of Au-S is about 2.559 Å. The rest of two thiol functional group adoptions tend to adsorb on bridge site. According to the XPS analysis, the thioether binding structure is the majority of the adsorption state. For the complexes adsorptions, we will only consider this configuration.

6.4.3. $[\text{Ni}(\mu_3 - \text{Cl})\text{Cl}(\text{HL} \cdot \text{S})]_x$ ($x = 1, 2, 3$) adsorption

Based on the geometry of the ligand adsorption, we simulate the $[\text{Ni}(\mu_3 - \text{Cl})\text{Cl}(\text{HL} \cdot \text{S})]_x$ ($x = 1, 2, 3$) adsorption on the Au (111) surface. The complexes strongly bind with the Au surface with an adsorption energies are -5.2, -5.1 and -5.3eV respectively.

After the complexes adsorb on the surface, the geometry, compared to the molecular data, barely change. The Ni-Ni distance of all these three configurations are listed in the Table 6.7. Their structures are shown in the Figure 6.7.

Table 6.7 Comparison between the molecular structural parameter of $[\text{Ni}(\mu_3 - \text{Cl})\text{Cl}]_4(\text{HL} \cdot \text{S})_x$ ($x = 1, 2, 3$) and after adsorption on surface. Bond distances are given in Å, $\text{Dis}_{\text{Ni-Ni}}$ stand for the distance between Ni atoms, $D_{\text{sur,mol}}$ is difference Ni-Ni distances between before and after adsorption

Dis _{Ni-Ni}	Ligand coordinated to Ni2			Ligands coordinated to Ni3 Ni4			Ligands coordinated to Ni2, Ni3, Ni4		
	mol	surface	$D_{\text{sur,mol}}$	mol	surface	$D_{\text{sur,mol}}$	mol	surface	$D_{\text{sur,mol}}$
Ni 1- Ni 2	3.649	3.564	-0.085	3.340	3.250	-0.090	3.562	3.454	-0.108
Ni 1- Ni 3	3.326	3.300	-0.026	3.384	3.271	-0.113	3.377	3.188	-0.189
Ni 1- Ni 4	3.353	3.275	-0.078	3.774	3.852	0.078	3.592	3.508	-0.084
Ni 2- Ni 3	3.718	3.632	-0.086	3.655	3.589	-0.066	3.839	3.775	-0.064
Ni 2- Ni 4	3.432	3.311	-0.121	3.629	3.678	0.049	3.763	3.691	-0.072
Ni 3- Ni 4	3.36	3.307	-0.053	3.780	3.638	-0.142	3.685	3.576	-0.109

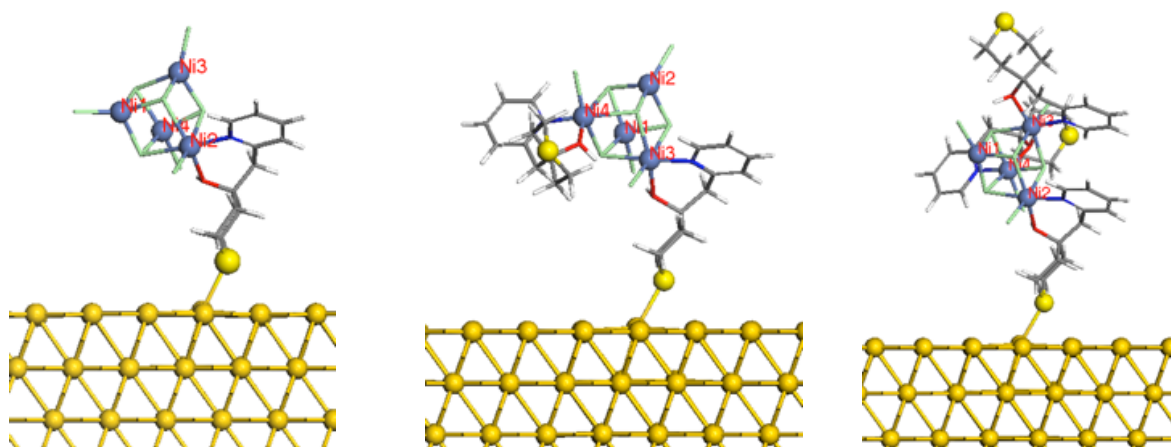


Figure 6.7 The structure of $[\text{Ni}(\mu_3 - \text{Cl})\text{Cl}]_4(\text{HL} \cdot \text{S})_x$ ($x = 1$ (a), 2 (b), 3(c)) adsorption on Au (111) surface

In general, the distances between Ni atoms change slightly, that main come from the different functional and convergence criteria.

During the optimization process, the $[\text{Ni}(\mu_3 - \text{Cl})\text{Cl}]_4(\text{HL} \cdot \text{S})_x$ ($x = 1,3$) successfully converge to the ferromagnetic solution with $S=4$, while $[\text{Ni}(\mu_3 - \text{Cl})\text{Cl}]_4(\text{HL} \cdot \text{S})_2$ converge to the intermediated spin-state ($S=2$). To be more specific, the magnetic moments are 7.8, 3.8, 7.9 receptively. That are in agreement with the molecular results. However, since the hard convergence for the constrained spin state calculation in VASP, and ill-description of PBE functional in tiny energy difference for such a big system, we are not capable to calculate the energy difference between spin-state at this stage.

6.5. Conclusion

In this work, we have studied the magnetic prosperities of $[\text{Ni}(\mu_3 - \text{Cl})\text{Cl}]_4(\text{HL} \cdot \text{S})_x$ ($x = 0,1,2,3,4$) complexes. The different spin state behavior is caused by the Ni unpaired electrons, ligand-field effects, and magnetic anisotropy characteristics arising from single-ion effects. In this report, the CASSCF calculation underestimate the J constants. However, the trend of the CASSCF results is correct.

In Ni_4Cl_8 complex, the J is close to zero, which lead to a $S=0$ ground state. The complex could be paramagnetic as same behavior as $[\text{NiCl}_4]^{2-}$.

In the $\text{Ni}_4\text{Cl}_8(\text{HLS})_x$ system, the number of ligands affects the magnetic properties. When $n=1,3,4$ the calculated J constants (CASSCF level) are positive, leading to $S=4$ ground state. The higher coordination number is; the stronger interaction is the complex.

When the complexes adsorb on the Au (111) surface, the distance between Ni atoms change slightly. The magnetic properties are supposed to remain the same to the molecular results.

Conclusions

In first part of work, we have studied the NO dissociation on Ru (0001) surface, and the external electric field effect for this process; NO dissociation on Ru (10 $\bar{1}$ 5) step surface, and more open flat Ru (10 $\bar{1}$ 0) surface. This process is essentially important to the NO_x reduce and environment related issues. We have used DFT to describe the model of NO dissociation to simulation the reduction process of NO molecule on different Ru surfaces.

We firstly studied the NO dissociation on Ru (0001) surface, and use these results as reference. The results are in good agreement with previous studies [3,4], that justifies our research method. The hcp site is determined to possess relatively higher reactivity on the Ru (0001) surface for NO dissociation. Since the hcp site is more active than fcc site, the atomic species can easily diffuse from fcc sites to hcp sites, leading a higher coverage of atomic species at hcp site.

When the external electric field is applied, the negative field yield an improvement for the NO dissociation on Ru (0001) surface. That is mainly attributed to the fact that the negative field decrease the NO adsorption on Ru (0001) surface. In contrast, when the external electric field is positive, the activation barrier remains almost same to the results without electric field.

In addition, we have studied NO dissociation on stepped Ru surfaces. Since previous step model of Ru surface may not describe correctly, we proposed to use step (10 $\bar{1}$ 5) and step (10 $\bar{1}$ 9) surface to study the step effect. The NO can easily dissociate on the step site. The dissociated atomic species, to be more specific atomic oxygen, strongly bind with the step site, leading a self-poisoning for the further reaction. For the terrace, it mainly remains the same reactive properties to flat Ru (0001) surface.

In fact, the step (10 $\bar{1}$ 9) surface has been found to reconstruct in experiment, that the one-layer step in ideal (10 $\bar{1}$ 9) surface will construct a double-layer step. The two-layer step is (10 $\bar{1}$ 0) surface. Based on this fact, we further investigated the NO dissociation on Ru (10 $\bar{1}$ 0) surface. For the NO dissociation on Ru (10 $\bar{1}$ 0) surface, the parallel adsorption states, due to their geometries, have advantage to dissociate the NO molecule over vertical adsorption states. The NO dissociation barrier on fourfold sites (parallel adsorption) are only about 0.1 – 0.2 eV. For the oxygen atomic adsorption, there is small energy difference among all the adsorption site and it can easily diffuse on the Ru (10 $\bar{1}$ 0) surface. The Ru (10 $\bar{1}$ 0), compared to the step surface, has more active sites for NO dissociation. Moreover, Ru (10 $\bar{1}$ 0) surface is more active than flat Ru (0001) surface for NO dissociation.

In the second part of work done in Groningen, we have studied the magnetic prosperities of [Ni($\mu_3 - \text{Cl}$)Cl]₄(HL · S)_x (x = 0,1,2,3,4) complexes. The different spin state behavior caused by the Ni unpaired electrons, ligand-field effects, and magnetic anisotropy characteristics arising from single-ion effects. In this report, the CASSCF calculation underestimate the J constants. However, the tend of the CASSCF results is correct.

In Ni₄Cl₈ complex, the J is close to zero, which lead to a S=0 ground state. The complex could be paramagnetic as same behavior as [NiCl₄]²⁻.

In the $\text{Ni}_4\text{Cl}_8(\text{HLS})_x$ system, the number of ligands affects the magnetic properties. When $n=1,3,4$ the calculated J constants (CASSCF level) are positive, leading to $S=4$ ground state. The higher coordination number is; the stronger interaction is the complex.

When the complexes adsorb on the Au (111) surface, the distance between Ni atoms change slightly. The magnetic properties are supposed to remain the same to the molecular results.

Reference:

1. Sutter, John D.; Berlinger, Joshua (12 December 2015). "Final draft of climate deal formally accepted in Paris". CNN. Cable News Network, Turner Broadcasting System, Inc. Retrieved 12 December 2015.
2. <http://www.autoblog.com/2015/09/18/volkswagen-diesel-federal-charges/>
3. Hammer, B. (2000). Adsorption, diffusion, and dissociation of NO, N and O on flat and stepped Ru(0001). *Surface Science*, 459(3), 323–348. doi:10.1016/S0039-6028(00)00467-2
4. Hammer, B. (1999). Bond Activation at Monatomic Steps: NO Dissociation at Corrugated Ru(0001). *Physical Review Letters*, 83(18), 3681–3684. doi:10.1103/PhysRevLett.83.3681
5. Gajdoš, M., Hafner, J., & Eichler, A. (2005). density-functional study of NO on close-packed transition and noble metal surfaces: I. Molecular adsorption. *Journal of Physics: Condensed Matter*, 18, 13–40. doi:10.1088/0953-8984/18/1/002
6. Dahl, S., Logadottir, a., Egeberg, R., Larsen, J., Chorkendorff, I., Törnqvist, E., & Nørskov, J. (1999). Role of Steps in N₂ Activation on Ru(0001). *Physical Review Letters*, 83(9), 1814–1817. doi:10.1103/PhysRevLett.83.1814
7. Zambelli, T., Wintterlin, J., Trost, J., & Ertl, G. (1996). Identification of the “Active Sites” of a Surface-Catalyzed Reaction. *Science*, 273(5282), 1688–1690. doi:10.1126/science.273.5282.1688
8. Falsig, H., Bligaard, T., Christensen, C. H., & Nørskov, J. K. (2007). Direct NO decomposition over stepped transition-metal surfaces. *Pure and Applied Chemistry*, 79(11), 1895–1903. doi:10.1351/pac200779111895
9. Liu, Z. P., Jenkins, S. J., & King, D. a. (2003). Step-Enhanced Selectivity of NO Reduction on Platinum-Group Metals. *Journal of the American Chemical Society*, 125, 14660–14661. doi:10.1021/ja0372208
10. Liu, Z.-P., & Hu, P. (2004). CO oxidation and NO reduction on metal surfaces: density functional theory investigations. *Top. Catal.*, 28(April), 71. Retrieved from <http://link.springer.com/article/10.1023/B:TOCA.0000024335.88459.81>
11. Tsukahara, N., Mukai, K., Yamashita, Y., Yoshinobu, J., & Aizawa, H. (2006). Adsorption states of NO on the Pt(111) step surface. *Surface Science*, 600(17), 3477–3483. doi:10.1016/j.susc.2006.06.040
12. Varganov, S. a., Olson, R. M., Gordon, M. S., & Metiu, H. (2003). The interaction of oxygen with small gold clusters. *The Journal of Chemical Physics*, 119(5), 2531. doi:10.1063/1.1587115
13. Hong, S., Rahman, T. S., Jacobi, K., & Ertl, G. (2007). Interaction of NO with RuO₂(110) surface: a first principles study. *The Journal of Physical Chemistry C*, 111(33), 12361–12368.
14. Wang, H., & Schneider, W. F. (2011). Adsorption and reactions of NO_x on RuO₂(110). *Catalysis Today*, 165(1), 49–55. doi:10.1016/j.cattod.2010.11.046
15. Fan, Chao Yang, et al. "The oxidation of CO on RuO₂ (110) at room temperature." *The Journal of Chemical Physics* 114.22 (2001): 10058-10062.
16. Wang, Jinhai, et al. "Adsorption and reaction of CO on RuO₂ (110) surfaces." *Surface science* 481.1 (2001): 113-118.
17. Wang, Y., Jacobi, K., & Ertl, G. (2003). Interaction of NO with the Stoichiometric RuO₂ (110) Surface. *The Journal of Physical Chemistry B*, 107(50), 13918–13924. doi:10.1021/jp0308108

18. Bandarenka, A. S., & Koper, M. T. M. (2013). Structural and electronic effects in heterogeneous electrocatalysis: Toward a rational design of electrocatalysts. *Journal of Catalysis*, *308*, 11–24. doi:10.1016/j.jcat.2013.05.006
19. De Groot, M. T., Merckx, M., & Koper, M. T. M. (2005). Heme release in myoglobin-DDAB films and its role in electrochemical NO reduction. *Journal of the American Chemical Society*, *127*(46), 16224–16232. doi:10.1021/ja0546572
20. De Vooy, a. C. a, Beltramo, G. L., Van Riet, B., Van Veen, J. a R., & Koper, M. T. M. (2004). Mechanisms of electrochemical reduction and oxidation of nitric oxide. *Electrochimica Acta*, *49*(8), 1307–1314. doi:10.1016/j.electacta.2003.07.020
21. de Vooy, A. C. ., Koper, M. T. ., van Santen, R. ., & van Veen, J. A. . (2001). Mechanistic Study on the Electrocatalytic Reduction of Nitric Oxide on Transition-Metal Electrodes. *Journal of Catalysis*, *202*(2), 387–394. doi:10.1006/jcat.2001.3275
22. Editor, G., Russell, A., Shen, Y., Träuble, M., Wittstock, G., Wasileski, S. A., ... Chem, P. (2008). Electrocatalysis: theory and experiment at the interface. *Physical Chemistry Chemical Physics*, *10*(25), 3607. doi:10.1039/b808799g
23. Koper, M. (2001). Mechanistic study of the nitric oxide reduction on a polycrystalline platinum electrode. *Electrochimica Acta*, *46*, 923– 930. doi:10.1016/S0013-4686(00)00678-2
24. Koper, M. T. ., & van Santen, R. a. (1999). Electric field effects on CO and NO adsorption at the Pt(111) surface. *Journal of Electroanalytical Chemistry*, *476*(1), 64–70. doi:10.1016/S0022-0728(99)00367-8
25. Koper, M. T. M., van Santen, R. a., Wasileski, S. a., & Weaver, M. J. (2000). Field-dependent chemisorption of carbon monoxide and nitric oxide on platinum-group (111) surfaces: Quantum chemical calculations compared with infrared spectroscopy at electrochemical and vacuum-based interfaces. *The Journal of Chemical Physics*, *113*(10), 4392. doi:10.1063/1.1288592
26. Rosca, V., Beltramo, G. L., & Koper, M. T. M. (2005). Reduction of NO adlayers on Pt(110) and Pt(111) in acidic media: evidence for adsorption site-specific reduction. *Langmuir : The ACS Journal of Surfaces and Colloids*, *21*(4), 1448–56. doi:10.1021/la0475831
27. Wasileski, S. a., Koper, M. T. M., & Weaver, M. J. (2001). Field-Dependent Chemisorption of Carbon Monoxide on Platinum-Group (111) Surfaces: Relationships between Binding Energetics, Geometries, and Vibrational Properties as Assessed by Density Functional Theory. *The Journal of Physical Chemistry B*, *105*(17), 3518–3530. doi:10.1021/jp003263o
28. Kreuzer, H. J., & Wang, L. C. (1990). Field-induced surface chemistry of NO. *The Journal of Chemical Physics*, *93*(8), 6065. doi:10.1063/1.459494
29. Hohenberg, Pierre, and Walter Kohn. "Inhomogeneous electron gas." *Physical review* *136.3B* (1964): B864.
30. Kohn, Walter, and Lu Jeu Sham. "Self-consistent equations including exchange and correlation effects." *Physical review* *140.4A* (1965): A1133.
31. Perdew, John P., Kieron Burke, and Matthias Ernzerhof. "Generalized gradient approximation made simple." *Physical review letters* *77.18* (1996): 3865.
32. Perdew, John P., et al. "Atoms, molecules, solids, and surfaces: Applications of the generalized gradient approximation for exchange and correlation." *Physical Review B* *46.11* (1992): 6671.
33. Vanderbilt, David. "Soft self-consistent pseudopotentials in a generalized eigenvalue formalism." *Physical Review B* *41.11* (1990): 7892.
34. Troullier, Norman, and José Luís Martins. "Efficient pseudopotentials for plane-wave calculations." *Physical review B* *43.3* (1991): 1993.
35. Kresse, Georg, and D. Joubert. "From ultrasoft pseudopotentials to the projector augmented-wave method." *Physical Review B* *59.3* (1999): 1758.
36. Pulay, Peter. "Convergence acceleration of iterative sequences. The case of SCF iteration." *Chemical Physics Letters* *73.2* (1980): 393-398.
37. Press, William H., et al. "Numerical Recipes (Cambridge." (1992).

38. Henkelman, Graeme, Blas P. Uberuaga, and Hannes Jónsson. "A climbing image nudged elastic band method for finding saddle points and minimum energy paths." *The Journal of chemical physics* 113.22 (2000): 9901-9904.
39. Henkelman, Graeme, and Hannes Jónsson. "Improved tangent estimate in the nudged elastic band method for finding minimum energy paths and saddle points." *The Journal of chemical physics* 113.22 (2000): 9978-9985.
40. Sheppard, Daniel, Rye Terrell, and Graeme Henkelman. "Optimization methods for finding minimum energy paths." *The Journal of chemical physics* 128.13 (2008): 134106.
41. Tang, W., E. Sanville, and G. Henkelman. "A grid-based Bader analysis algorithm without lattice bias." *Journal of Physics: Condensed Matter* 21.8 (2009): 084204.
42. Kresse, G. and J. Furthmüller, *Efficient iterative schemes for ab initio total-energy calculations using a plane-wave basis set*. Physical Review B, 1996. **54**(16): p. 11169.
43. Kresse, G. and J. Furthmüller, *Efficiency of ab-initio total energy calculations for metals and semiconductors using a plane-wave basis set*. Computational Materials Science, 1996. **6**(1): p. 15-50.
44. Murnaghan, F. D. "The compressibility of media under extreme pressures." *Proceedings of the National Academy of Sciences* 30.9 (1944): 244-247.
45. Villars, P., L. D. Calvert, and W. B. Pearson. "Handbook of crystallographic data for intermetallic phases." *Acta Crystallographica Section A*. Vol. 40. 35 NORRE SOGADE, PO BOX 2148, DK-1016 COPENHAGEN, DENMARK: MUNKSGAARD INT PUBL LTD, 1984.
46. Murnaghan, F. D. "The compressibility of media under extreme pressures." *Proceedings of the National Academy of Sciences* 30.9 (1944): 244-247.
47. Feibelman, Peter J., et al. "Relaxation of the clean, Cu-and H-covered Ru (0001) surface." *Surface science* 302.1 (1994): 81-92.
48. Hammer, B. "Bond activation at monatomic steps: NO dissociation at corrugated Ru (0001)." *Physical review letters* 83.18 (1999): 3681.
49. Hammer, B. "Adsorption, diffusion, and dissociation of NO, N and O on flat and stepped Ru (0001)." *Surface science* 459.3 (2000): 323-348.
50. Gajdoš, Marek, Jürgen Hafner, and Andreas Eichler. "Ab initio density-functional study of NO on close-packed transition and noble metal surfaces: I. Molecular adsorption." *Journal of Physics: Condensed Matter* 18.1 (2005): 13.
51. Gajdoš, Marek, Jürgen Hafner, and Andreas Eichler. "Ab initio density-functional study of NO adsorption on close-packed transition and noble metal surfaces: II. Dissociative adsorption." *Journal of Physics: Condensed Matter* 18.1 (2005): 41.
52. Lindroos, M., et al. "Adsorbate induced reconstruction by strong chemisorption: Ru (001) p (2×2)-O." *Surface Science* 222.2 (1989): 451-463.
53. Stampfl, Catherine, and Matthias Scheffler. "Theoretical study of O adlayers on Ru (0001)." *Physical Review B* 54.4 (1996): 2868.
54. Renisch, Steffen, et al. "Dynamics of adatom motion under the influence of mutual interactions: O/Ru (0001)." *Physical review letters* 82.19 (1999): 3839.
55. Dahl, Søren, et al. "Role of steps in N₂ activation on Ru (0001)." *Physical Review Letters* 83.9 (1999): 1814.
56. 4.Zambelli, T., Wintterlin, J., Trost, J., & Ertl, G. (1996). Identification of the "Active Sites" of a Surface-Catalyzed Reaction. *Science*, 273(5282), 1688–1690. doi:10.1126/science.273.5282.1688
57. 5.Lischka, M., Mosch, C., & Groß, A. (2007). Tuning catalytic properties of bimetallic surfaces: Oxygen adsorption on pseudomorphic Pt/Ru overlayers. *Electrochimica Acta*, 52(6), 2219–2228. doi:10.1016/j.electacta.2006.03.113

58. 6. Alayoglu, S., Nilekar, A. U., Mavrikakis, M., & Eichhorn, B. (2008). Ru-Pt core-shell nanoparticles for preferential oxidation of carbon monoxide in hydrogen. *Nature Materials*, 7(4), 333–338. doi:10.1038/nmat2156
59. 7. Granger, P., & Parvulescu, V. I. (2011). Catalytic NO_x abatement systems for mobile sources: From three-way to lean burn after-treatment technologies. *Chemical Reviews*, 111(5), 3155–3207. doi:10.1021/cr100168g
60. Koper, M. T. ., & van Santen, R. a. (1999). Electric field effects on CO and NO adsorption at the Pt(111) surface. *Journal of Electroanalytical Chemistry*, 476(1), 64–70. doi:10.1016/S0022-0728(99)00367-8
61. Zubkov, Tykhon, Gregg A. Morgan, and John T. Yates. "Spectroscopic detection of CO dissociation on defect sites on Ru (109): implications for Fischer–Tropsch catalytic chemistry." *Chemical physics letters* 362.3 (2002): 181-184.
62. Ku, R. N. A. H. P., N. A. Gjostein, and H. P. Bonzel. "Adsorption of NO and CO on a Ru (1010) surface." *Surface Science* 64.2 (1977): 465-483.
63. Bonzel, H. P., and T. E. Fischer. "An UV photoemission study of No and CO adsorption on Pt (100) and Ru (1010) surfaces." *Surface Science* 51.1 (1975): 213-227.
64. Ghisolfi, Alessio, et al. "A comparative synthetic, magnetic and theoretical study of functional M₄Cl₄ cubane-type Co (ii) and Ni (ii) complexes." *Dalton transactions* 43.21 (2014): 7847-7859.
65. Heß, Volkmar, et al. "Adsorption phenomena of cubane-type tetranuclear Ni (II) complexes with neutral, thioether-functionalized ligands on Au (111)." *Surface science* 641 (2015): 210-215.
66. Neese, Frank. "The ORCA program system." *Wiley Interdisciplinary Reviews: Computational Molecular Science* 2.1 (2012): 73-78.
67. Stephens, P. J., et al. "Ab initio calculation of vibrational absorption and circular dichroism spectra using density functional force fields." *The Journal of Physical Chemistry* 98.45 (1994): 11623-11627.
68. Grimme, Stefan, et al. "A consistent and accurate ab initio parametrization of density functional dispersion correction (DFT-D) for the 94 elements H-Pu." *The Journal of chemical physics* 132.15 (2010): 154104.
69. Marenich, Aleksandr V., Christopher J. Cramer, and Donald G. Truhlar. "Universal solvation model based on solute electron density and on a continuum model of the solvent defined by the bulk dielectric constant and atomic surface tensions." *The Journal of Physical Chemistry B* 113.18 (2009): 6378-6396.
70. Weigend, Florian. "Accurate Coulomb-fitting basis sets for H to Rn." *Physical chemistry chemical physics* 8.9 (2006): 1057-1065.
71. Calzado, Carmen J., et al. "Analysis of the magnetic coupling in nitroxide organic biradicals." *Theoretical Chemistry Accounts* 128.4-6 (2011): 505-519.